

Jahn-Teller effect in cubic fullerenes A_3C_{60}

Zhishuo Huang,¹ Munirah D. Albaqami,² Tohru Sato,³ Naoya Iwahara,^{4,1,5,*} and Liviu F. Chibotaru^{1,†}

¹*Theory of Nanomaterials Group, KU Leuven, Celestijnenlaan 200F, B-3001 Leuven, Belgium*

²*Chemistry Department, College of Science, King Saud University, P.O. Box 2455, Riyadh 11451, Saudi Arabia*

³*Fukui Institute for Fundamental Chemistry, Kyoto University,
Takano Nishihiraki-cho 34-4, Sakyo-ku, Kyoto 6068103, Japan*

⁴*Department of Chemistry, National University of Singapore,
Block S8 Level 3, 3 Science Drive 3, 117543, Singapore*

⁵*Graduate School of Engineering, Chiba University,
1-33 Yayoi-cho, Inage-ku, Chiba 263-8522, Japan*

(Dated: March 26, 2021)

Compared to isolated C_{60}^{3-} ions, characterized by a three-dimensional equipotential trough at the bottom of the lowest adiabatic potential energy surface (APES), the Jahn-Teller (JT) effect in cubic fullerenes is additionally influenced by the interaction of JT distortions at C_{60} sites with vibrational modes of the lattice. This leads to modification of JT stabilization energy and to the warping of the trough at each fullerene site, as well as to the interaction of JT distortions at different sites. Here we investigate these effects in three fcc fullerenes with $A=K,Rb,Cs$ and in Cs_3C_{60} with bcc (A15) structure. DFT calculations of orbital vibronic coupling constants at C_{60} sites and of phonon spectra have been done for fully ordered lattices (1 C_{60} /u.c.). Based on them the elastic response function for local JT distortions has been evaluated and the lowest APES investigated. To this end an expression for the latter in function of trough coordinates of all sites has been derived. The results show that the JT stabilization energy slightly increases compared to an isolated C_{60}^{3-} and a warping of the trough of few meV occurs. The interaction of JT distortions on nearest- and next-nearest-neighbor fullerene sites is of similar order of magnitude. These effects arise first of all due to the interaction of C_{60} sites with the displacements of neighbor alkali atoms and are more pronounced in fcc fullerenes than in the A15 compound. The results of this study support the picture of weakly hindered independent rotations of JT deformations at C_{60} sites in cubic A_3C_{60} .

I. INTRODUCTION

Cubic alkali-doped fullerenes A_3C_{60} ($A = K, Rb, Cs$) have attracted much attention due to a large variety of unusual electronic properties, such as the superconductivity in equilibrium [1–5] and in nonequilibrium [6, 7] states and the metal-insulator transition controlled by the carrier concentration n (number of electrons in the LUMO band) [1, 8, 9], type of alkali atom A and applied pressure [3–5, 10]. The electronic properties of these materials are strongly influenced by the Jahn-Teller (JT) effect on fullerene sites, notably the superconductivity, for which it represents the main mechanism of Cooper pairing. One should stress that A_3C_{60} superconductors are remarkable in several respects. They are high- T_c superconductors with a highest critical temperature ($T_c = 38$ K for $A = Cs$) among organic superconductors. Recently a transient superconductivity with a critical temperature exceeding many times its value at equilibrium was found in K_3C_{60} [6, 7, 11]. In addition these are the only superconducting materials with JT mechanism of pairing [comment]. Finally, the JT effect in these fullerenes is dynamic due to a threefold orbital degeneracy of fullerene sites C_{60}^{3-} imposed by their cubic site symmetry, which persists also in metallic compounds [12, 13].

The Jahn-Teller effect in fullerene ions was thoroughly investigated during the last decades. With increased accuracy of DFT methods and well resolved photoemission bands, the value of Jahn-Teller stabilization energy in an isolated anion C_{60}^{3-} was firmly established [14]. Recently, by applying a novel exchange-correlation functional, the theoretical reproduction of the magnitude of vibronic coupling constants for active vibrational modes nH_g , $n=1-8$, became possible [15]. At the same time, the Jahn-Teller effect on fullerene sites in fullerene materials was not investigated yet.

Compared to isolated fullerene molecules, the JT effect on C_{60} sites in fullerenes is expected to be more complex. Thus, although the strength of vibronic coupling to intra fullerene vibrational modes is not expected to be significantly modified compared to isolated molecules (this is confirmed by the present calculations), the five-fold degenerate active vibrational modes themselves split into threefold and twofold degenerate modes each, $H_g = T_g + E_g$ due to the symmetry reduction from I_h to T_h group [16] when the fullerene is placed in a cubic crystal. This effect gives a contribution to the warping of the two-dimensional rotational trough of the adiabatic potential of the corresponding $T \times h$ vibronic problem (actually of a three-dimensional rotational trough in the case of C_{60}^{3-}). Second, the nearest environment of a C_{60} molecule in a cubic crystal (nearest-neighbour alkali atoms and fullerene molecules) provides additional JT active nuclear modes which can modify the local Jahn-Teller effect on sites. Finally, the active JT modes at neighbor fullerene

* naoya.iwahara@gmail.com

† liviu.chibotaru@kuleuven.be

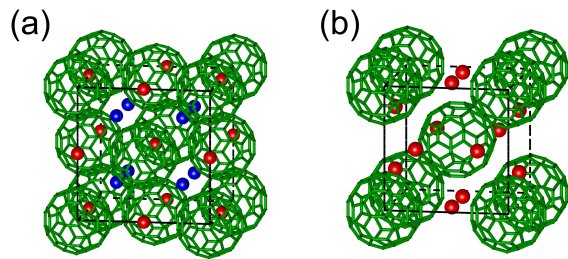


FIG. 1. Crystal structures of A_3C_{60} . C_{60} molecules are depicted by the green framework. (a). Fcc unit cell; alkali atoms sitting in octahedral and tetrahedral interstitials are shown by red and blue balls. (b). Bcc-like unit cell for A15 structure; Cs atoms are indicated by red balls.

sites interact with each other through common phonon modes thus hindering or, eventually blocking the free rotation of Jahn-Teller deformations on individual fullerene sites. Despite the importance, the strength of these three effects was never estimated in fullerides. On the other hand the quantitative knowledge of these effects will allow to conclude on the character of JT effect on fullerene sites in A_3C_{60} .

Despite intensive experimental research [17–19], it is proved to be hardly conclusive on the details of intrasite vibronic interactions due to the superposition of additional effects influencing the spectroscopic bands in fullerides. On the contrary, given the success of DFT investigation of JT effect in individual fullerene ions, we expect that a similar methodology could shed light on its manifestation in fullerides. In the present work, the the Jahn-Teller effect on fullerene sites in A_3C_{60} is thoroughly investigated fully taking into account the effects mentioned above.

II. VIBRONIC INTERACTION IN CUBIC FULLERIDES

Cubic A_3C_{60} crystalize into face-centered cubic (fcc) and body-centered cubic (bcc) structures (Fig. 1). In both types of A_3C_{60} , one electron from each alkali atom A transfers to the t_{1u} LUMO orbitals of fullerenes, due to a very strong electronegativity of the latter, resulting in their three-fold population at each C_{60} site. Since all fullerene molecules reside in cubic lattice points, their symmetry is reduced from I_h to T_h point group, implying that the t_{1u} orbitals keep their three-fold degeneracy (belonging now to the T_u irrep of the T_h group). At the same time the icosahedral irrep H_g splits under this symmetry reduction into E_g and T_g [16].

In the following we consider the simplest situation of fully localized LUMO electrons at sites.

A. The Jahn-Teller Hamiltonian for localized LUMO electrons at C_{60} sites

The JT Hamiltonian for A_3C_{60} reads as follows:

$$\hat{H}_{JT} = \hat{H}_{ph} + \sum_{\mathbf{n}} \left(\hat{H}_U^{\mathbf{n}} + \hat{H}_H^{\mathbf{n}} + \hat{V}_a^{\mathbf{n}} + \hat{V}_e^{\mathbf{n}} + \hat{V}_t^{\mathbf{n}} \right). \quad (1)$$

The first term is the phonon Hamiltonian of the crystal,

$$\hat{H}_{ph} = \sum_{\kappa\mathbf{k}} \left(\frac{1}{2} \hat{P}_{\kappa\mathbf{k}}^2 + \frac{1}{2} \omega_{\kappa\mathbf{k}}^2 Q_{\kappa\mathbf{k}}^2 \right), \quad (2)$$

expressed via phonon coordinates $Q_{\kappa\mathbf{k}}$ characterized by the wave vector \mathbf{k} and the branch κ . The other terms in (1) are one-site contributions with \mathbf{n} denoting the unit cell which is supposed to include one A_3C_{60} formula unit. $\hat{H}_U^{\mathbf{n}}$ and $\hat{H}_H^{\mathbf{n}}$ describe bielectronic interactions in the LUMO orbitals of \mathbf{n} -th fullerene molecule:

$$\begin{aligned} \hat{H}_U^{\mathbf{n}} &= \sum_{\alpha} \sum'_{\beta(\neq\alpha)} \sum_{\sigma} \frac{U_{\perp}}{2} \hat{n}_{\alpha\sigma} \hat{n}_{\beta\sigma} + \sum_{\alpha\sigma} \frac{U_{\perp}}{2} \hat{n}_{\alpha\sigma} \hat{n}_{\alpha-\sigma} \\ &= \frac{U_{\perp}}{2} \left(\hat{N}^2 - \hat{N} \right), \\ \hat{H}_H^{\mathbf{n}} &= \sum_{\alpha} \sum'_{\beta(\neq\alpha)} \sum_{\sigma} \frac{J_H}{2} \left[-\hat{n}_{\alpha\sigma} \hat{n}_{\beta\sigma} + \hat{c}_{\alpha\sigma}^{\dagger} \hat{c}_{\beta\sigma} \hat{c}_{\alpha-\sigma}^{\dagger} \hat{c}_{\beta-\sigma} \right. \\ &\quad \left. + \hat{c}_{\alpha\sigma}^{\dagger} \hat{c}_{\beta\sigma} \hat{c}_{\alpha-\sigma}^{\dagger} \hat{c}_{\beta-\sigma} \right] + \sum_{\alpha\sigma} J_H \hat{n}_{\alpha\sigma} \hat{n}_{\alpha-\sigma}, \end{aligned} \quad (3)$$

where the second-quantization operators correspond to the LUMO orbitals of the corresponding fullerene site, $\alpha, \beta = x, y, z$, and $\hat{N} = \sum_{\alpha\sigma} \hat{n}_{\alpha\sigma}$ is the operator of total number of electrons in the t_{1u} shell. The first term is the Coulomb repulsion of LUMO electrons, the parameter U_{\perp} describing the repulsion of electrons in different orbitals within the same t_{1u} shell. Since this contribution depends only on the total number of LUMO electrons on site considered constant in the present work, it gives only a constant energy shift and is dropped in the subsequent treatment. The term $\hat{H}_H^{\mathbf{n}}$ describes orbitally-specific electronic interactions which, due to the isomorphism of cubic t_{1u} and atomic p shells, depend on one Hund's parameter J_H . Besides exchange (Hund's rule) coupling and electron pairs transfer between different t_{1u} orbitals, this operator also includes (through the last term) the difference between the electron repulsion in the same and different orbitals, $U_{\parallel} - U_{\perp} = 2J_H$.

The last three terms in the sum in Eq.(1) describe the vibronic interaction with three types of nuclear distortions at a given site, with irreps (of the T_h group) contained in the symmetric square $[T_u^2] = A_g \oplus E_g \oplus T_g$ [20],

$$\begin{aligned}
\hat{V}_A^{\mathbf{n}} &= \sum_{\mu} V_{\mu A} q_{\mu A}^{\mathbf{n}} \hat{N}, \\
\hat{V}_E^{\mathbf{n}} &= \sum_{\sigma} \sum_{\mu} V_{\mu E} (\hat{c}_{x\sigma}^{\dagger}, \hat{c}_{y\sigma}^{\dagger}, \hat{c}_{z\sigma}^{\dagger}) \begin{pmatrix} \frac{1}{2} q_{\mu\theta}^{\mathbf{n}} - \frac{\sqrt{3}}{2} q_{\mu\epsilon}^{\mathbf{n}} & 0 & 0 \\ 0 & \frac{1}{2} q_{\mu\theta}^{\mathbf{n}} + \frac{\sqrt{3}}{2} q_{\mu\epsilon}^{\mathbf{n}} & 0 \\ 0 & 0 & -q_{\mu\theta}^{\mathbf{n}} \end{pmatrix} \begin{pmatrix} \hat{c}_{x\sigma} \\ \hat{c}_{y\sigma} \\ \hat{c}_{z\sigma} \end{pmatrix}, \\
\hat{V}_T^{\mathbf{n}} &= \sum_{\sigma} \sum_{\mu} V_{\mu T} (\hat{c}_{x\sigma}^{\dagger}, \hat{c}_{y\sigma}^{\dagger}, \hat{c}_{z\sigma}^{\dagger}) \begin{pmatrix} 0 & \frac{\sqrt{3}}{2} q_{\mu\zeta}^{\mathbf{n}} & \frac{\sqrt{3}}{2} q_{\mu\eta}^{\mathbf{n}} \\ \frac{\sqrt{3}}{2} q_{\mu\zeta}^{\mathbf{n}} & 0 & \frac{\sqrt{3}}{2} q_{\mu\xi}^{\mathbf{n}} \\ \frac{\sqrt{3}}{2} q_{\mu\eta}^{\mathbf{n}} & \frac{\sqrt{3}}{2} q_{\mu\xi}^{\mathbf{n}} & 0 \end{pmatrix} \begin{pmatrix} \hat{c}_{x\sigma} \\ \hat{c}_{y\sigma} \\ \hat{c}_{z\sigma} \end{pmatrix}, \tag{4}
\end{aligned}$$

where $q_{\mu\gamma}^{\mathbf{n}}$ are symmetrized distortions at the \mathbf{n} -th fullerene site transforming after the row γ of the corresponding irrep; μ counts the repeating distortions of a given type. The latter include both distortions of the fullerene itself and displacements of surrounding atoms.

The operator \hat{V}_A depends on the total population number, i.e., a constant in the electronic space. It doesn't lead to the splitting of the t_{1u} orbitals and merely represents a constant force acting on the environment of the \mathbf{n} -th site in a totally symmetric fashion, i.e. without destroying its cubic site symmetry. Summed up over all sites, the effect of such terms results in the reoptimization of the structure of the cubic crystal, which is assumed to be already done during quantum chemistry calculations.

The other two operators describe the JT coupling to the local distortions at the \mathbf{n} -th site. Under the symmetry reduction $I_h \rightarrow T_h$, two of five symmetrized functions of the irrep H_g , $\gamma = \theta, \epsilon$, form the basis of the irrep E_g , while the other three, $\gamma = \xi, \eta, \zeta$, - of the irrep T_g . Then the Clebsch-Gordan coefficients [the numerical coefficients in two matrices in (4)] coincide for the two groups: $\langle t\alpha | \Gamma\gamma t\beta \rangle = \langle t_1\alpha | H\gamma t_1\beta \rangle$, where $\Gamma = E, T$ and $\alpha, \beta = x, y, z$. Therefore, for equal vibronic coupling constants of two types, $V_{\mu E} = V_{\mu T}$, the matrix describing the JT coupling with five symmetrized nuclear distortions in (4) coincides with the one for the $t_{1u} \otimes H_g$ JT problem [21, 22].

The assumption of localized electrons in the LUMO orbitals of fullerene sites is valid for insulating cubic fullerenes Cs_3C_{60} in the A15 structure (bcc) and fcc lattice at ambient pressure, and in all expanded fullerenes such as, e.g., $\text{Li}_3\text{NH}_3\text{C}_{60}$ [23, 24]. It is a reasonable approximation in metallic fullerenes which are not far from Mott-Hubbard metal-insulator transition. These are the fcc Cs_3C_{60} under pressure, Rb_3C_{60} and several $\text{A}_x\text{A}'_{3-x}\text{C}_{60}$ compounds with different alkali atoms A and A'. As a matter of fact, an experimental proof for (dynamical) JT effect in Rb_3C_{60} is the detection of a spin gap in its NMR spectrum [25].

Another approximation, of a single C_{60} per unit cell, was adopted to reduce the unit cell to one formula unit because of complications with the calculation of phonon spectrum. This situation is strictly realized only in mixed compounds $\text{AA}'_2\text{C}_{60}$. All other fullerenes are characterized by different forms of meroheral arrangement of

C_{60} 's (their C_2 rotations around a cubic axis). Thus the A15 Cs_3C_{60} is characterized by the meroheral order (two C_{60} 's in a unit cell), while the three other fcc compounds investigated here are subject to meroheral disorder [26–28]. We believe that the neglect of meroheral arrangement will not affect the main conclusions of this study, the main reason being the high symmetry of the C_{60} balls.

B. Calculation of orbital vibronic coupling constants

The vibronic coupling constants at fullerene sites have been extracted from the splitting of three t_{1u} LUMO orbitals in function of the amplitude of active local nuclear distortions [?]. To this end, DFT calculations of A_nC_{60} clusters including nearest and next-nearest neighbor alkaline atoms and point charges replacing other alkaline atoms and fullerenes (Fig. 2) have been done with Gaussian09 package [30]. Hybrid B3LYP exchange correlation functional [31] and triple-zeta basis set (6-311G(d)) were employed. The three LUMO orbitals have been populated by three electrons with parallel spins. For given local nuclear distortions, ten calculations corresponding to their different amplitude have been performed. From them the slopes of LUMO orbital energies in vicinity of equilibrium point have been extracted via an interpolation procedure and vibronic coupling constants derived for a number of active JT modes making use of vibronic matrices from Eq. (4).

1. Intrafullerene modes

As active JT modes, the normal vibrational H_g modes of isolated C_{60} [32] have been chosen, which merely subdivide into E_g and T_g modes in cubic fullerenes. We also calculated the vibronic coupling constants for intrafullerene A_g modes. The explicit form of the corresponding nuclear displacements is given in the Supplementary Material (SM) [33]. We note that these modes are not vibrational eigenmodes in fullerenes and have been chosen for the sake of comparison with isolated C_{60}^{3-} . We could have considered arbitrary combinations of them as

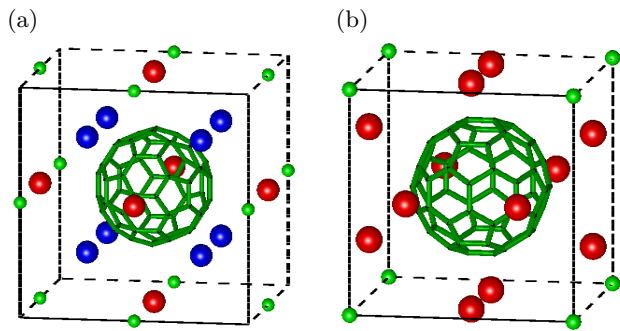


FIG. 2. A_nC_{60} fragments used for the calculation of vibronic coupling constants. (a) Fcc unit cell; octahedral and cubic alkali atoms are shown by red and blue balls. (b). Bcc-like unit cell (A15 structure); Cs atoms are indicated by red balls. Nearest neighbor C_{60} molecules contributing to interfullerene active JT modes are shown by green balls.

TABLE I. Vibronic coupling constants for E_g and T_g intrafullerene distortions of H_g genealogy compared to similar coupling constants in isolated C_{60}^- (in 10^{-6} a.u.).

	fcc								A15	
	K_3C_{60}		Rb_3C_{60}		Cs_3C_{60}		Cs_3C_{60}		C_{60}^-	
	E_g	T_g	E_g	T_g	E_g	T_g	E_g	T_g		
$H_g(1)$	18.9	19.9	19.2	19.8	19.4	19.4	19.0	19.7	19.2	
$H_g(2)$	42.4	39.9	43.4	41.0	44.4	42.3	44.4	43.0	45.0	
$H_g(3)$	80.1	78.7	80.2	78.9	80.4	79.5	81.0	79.0	75.4	
$H_g(4)$	56.3	53.0	56.6	53.3	56.7	53.9	54.8	55.6	55.4	
$H_g(5)$	77.5	77.2	76.1	76.8	74.8	76.3	75.1	75.3	76.6	
$H_g(6)$	58.1	58.5	58.6	58.9	58.9	59.4	58.1	59.8	57.8	
$H_g(7)$	200.4	202.3	199.9	203.7	299.7	204.7	201.2	204.0	209.9	
$H_g(8)$	206.1	201.5	205.4	202.4	204.7	203.3	205.0	203.5	204.3	
$A_g(1)$	66.7		67.8		70.2		70.0		26.4	
$A_g(2)$	311.8		310.5		308.7		309.5		238.0	

well because the resulting electron-phonon Hamiltonian is invariant with respect to any such choice.

The calculated vibronic coupling constants are shown in Table I.

Despite the molecular character of fulleride crystals, the difference between vibronic coupling constants for E_g and T_g modes appears to be non-negligible and these constants also differ from corresponding vibronic coupling constants of isolated fullerene ion (last column in Table I). We did not consider the coupling to intrafullerene modes of other I_h genealogy (G_g , T_{1g} and T_{2g}), which according to the selection rules for the T_h group also become active in fullerides. Because the coupling to these modes is absent for isolated fullerene anions, we expect it to be negligible in fullerides.

TABLE II. Vibronic coupling constants for symmetrized distortions of cubic (cub), octahedral (oct) frame of surrounding alkali atoms in fcc A_3C_{60} , and pseudo-octahedral (p-oct) frame in A15 (in 10^{-6} a.u.).

	fcc						A15
	K_3C_{60}		Rb_3C_{60}		Cs_3C_{60}		Cs_3C_{60}
	cub	oct	cub	oct	cub	oct	p-oct
$A_g(1)$	88.8	68.2	60.6	44.6	48.4	39.1	4.1
$E_g(1)$	2.6	2.4	1.6	1.5	1.0	1.1	1.8
$T_{2g}(1)$	2.7	0.8	2.0	0.5	1.7	0.4	0.9
$T_{2g}(2)$	0.2	-	0.2	-	0.1	-	0.9
$A_g(2)$	-	-	-	-	-	-	57.0
$E_g(2)$	-	-	-	-	-	-	0.8
$T_g(3)$	-	-	-	-	-	-	0.8

2. Alkali modes

In fcc A_3C_{60} each fullerene is surrounded by a cube of nearest neighbor and an octahedron of next-nearest neighbor alkali atoms (blue and red balls in Fig. 1a, respectively). The closest alkali environment contributes with one E_g and two T_g modes of symmetrized distortions, while the octahedral environment with one E_g and one T_g modes. The expressions of these modes via atomic displacements are given in SM [33] and also are depicted in various textbooks (see, e.g. [20]). In the case of A15 fulleride, the closest alkali atoms form a pseudo octahedron (two atoms at each face of surrounding cube) as shown in Fig. 1b. The active distortions include two E_g and two T_g modes whose form is given in SM [33].

The calculated vibronic coupling constants are given in Table II. As we can see, they are smaller than the vibronic coupling constants for intrafullerene modes by one order of magnitude (an exception are alkali A_g modes for fcc A_3C_{60}). Nevertheless these modes are related to acoustic and low-frequency optical phonons (see the next section), therefore their contribution to JT stabilization cannot be neglected from the start. Moreover, as will be seen below, their contribution is crucial for the warping of one-site APES and for the interaction of JT distortions at different sites.

3. Interfullerene modes

Each fullerene molecule in fcc A_3C_{60} is surrounded by twelve C_{60} 's forming a cub-octahedron (Fig. 2a). The latter yields two E_g and two T_g modes of symmetrized distortions. In A15 fulleride the nearest alkali atoms form a cube (Fig. 2b) which gives one E_g and two T_g modes. The expressions of these modes via atomic displacements are given in SM [33]. Given a large spacing between fullerene molecules, only the electrostatic interaction between them is taken into account in the calculation of

TABLE III. Vibronic coupling constants for active symmetrized distortions of fullerene molecules surrounding a given C_{60} in fcc and A15 fullerides (in 10^{-6} a.u.).

	fcc			A15
	K_3C_{60}	Rb_3C_{60}	Cs_3C_{60}	Cs_3C_{60}
A_g	35.1	34.3	32.5	27.7
$E_g(1)$	0.2	0.1	0.1	0.2
$E_g(2)$	0.2	0.2	0.2	-
$T_{2g}(1)$	0.2	0.2	0.2	0.3
$T_{2g}(2)$	0.3	0.3	0.2	0.1

vibronic coupling constants.

The calculated vibronic coupling constants are given in Table III. They are obtained one order of magnitude smaller than the vibronic coupling constants for alkali modes (Table II). This is because the interfullerene vibronic coupling can be seen as an electrostatic interaction of a set of electric dipoles (arising from shifted charges $q = 3e$) with the quadrupolar distribution of t_{1u} LUMO electrons, scaling as R^{-4} with a distance R to the center of C_{60} . On the other hand, there is an additional covalent contribution to vibronic coupling constants for alkali modes.

III. THE PHONON SPECTRUM OF CUBIC FULLERIDES

In order to take into account exactly the effect of the environment on the JT effect at fullerene sites and the intersite interaction of their active JT modes, the precise knowledge on phonon modes of A_3C_{60} is decisive. Many attempts have been undertaken to calculate the phonon dispersion. The first calculations by Varma *et al.* [Science 1991] and You *et al.* [34] in the beginning of 1990s were semiempirical but reflected qualitatively the basic features of phonon spectrum in A_3C_{60} fullerides. In spite of that, they could not achieve a correct description of intra-fullerene vibronic interaction. Later works [35, 36] with first principles methods also could not provide accurate information on the low-energy phonon modes: In these calculations, the low-energy frequencies become imaginary. In this work, this issue is solved by employing new ionized pseudopotentials for alkali atoms.

A. Calculation details

To reduce the calculational load, in both fcc and A15 fullerides the fullerenes were supposed to be completely ordered. Experimental lattice constants were used for the starting crystal structure [2, 3], then they are fully relaxed in order to get good phonon calculations. The phonon calculations have been done by density functional perturbation theory (DFPT) [37]

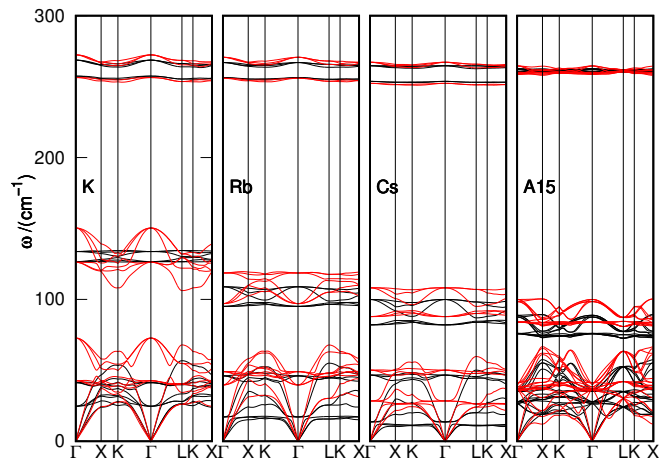


FIG. 3. Phonon dispersion for A_3C_{60} , including A15. Red and black lines correspond to PBE and LDA, respectively.

with exchange correlation functionals of LDA and PBE types [38, 39]. Given large unit cells in A_3C_{60} , soft pseudopotentials (PPs) have been employed. To this end, following Akashi and Arias[35], we chose the configuration $(3p)^{6.0}(4s)^{0.0}(3d)^{0.0}$, $(4p)^{6.0}(5s)^{0.0}(4d)^{0.0}$ and $(5p)^{6.0}(6s)^{0.0}(5d)^{0.0}$ for K, Rb, and Cs, respectively, with the nonlinear core correction [40]. The relativistic effects in alkali atoms were considered within scalar relativistic approximation [41]. All the PPs were generated by Trolled-Martins[42] method using atomic code within the plane wave based package Quantum Espresso [43]. For the LDA functional the parametrization of Perdew and Zunger (PZ) [38] was used and for the GGA functional the parametrization of Perdew, Burke, and Ernzerhof (PBE) [39] was employed. The details of generation of ionized PPs and the test calculations are given in SM [33].

The plane-wave kinetic energy cutoff was set to 60 Ry with the density cut-off of 240 Ry, and shifted $4 \times 4 \times 4$ Monkhorst-Pack meshes were used to perform Brillouin zone integration in order to ensure the convergence of the results. The convergence of the total energy was set to be better than 10^{-14} Hartree and forces on the atoms were limited within 10^{-5} Ry/a.u.

B. The phonon dispersion

The phonon dispersion for A_3C_{60} is shown in Fig. 3, where the frequency range was restricted to 300 cm^{-1} for visibility (see the SM [33] for the dispersion of all phonon bands). It is evident that no imaginary modes appear anymore in the present calculations with both PBE and LDA functionals, contrary to the previous calculations [35, 36].

Visualization of polarization vectors at the Γ point allows us to conclude that the lowest three optical branches, 4-6, correspond to opposite displacements of fullerene and a next nearest alkali atom, siting in the

octahedral interstitial, along three Cartesian axes. The next branches, 7-9, are three librational (pure rotational) modes of fullerene molecules. The next branches, 10-12, correspond to displacements of two nearest alkali atoms hybridized with $H_g\gamma(1)$ vibrations ($\gamma = \xi, \eta, \zeta$) of C_{60} cage. Finally the upper mixed branches, 7-15, represent opposite translations of two nearest alkali atoms and fullerene. All higher branches arise from almost pure intrafullerene vibrations. Thus the highest five bands in Fig. 3 correspond to $H_g(1)$ intrafullerene vibrations, split at the Γ point into E_g and T_g degenerate phonons according to cubic symmetry of the lattice.

Above 150 cm^{-1} , PBE gives slightly smaller frequencies than LDA albeit displaying similar dispersion, while in the lower frequency range, $0\div 150 \text{ cm}^{-1}$, the results of PBE and LDA disagree significantly. The calculated frequencies of the H_g intrafullerene phonons at the Γ point are tabulated in Table S2. One can see that the frequencies calculated by Nomura and Arita [36] with constrained DFPT within LDA are close to our results, and both are in a good agreement with the experimental Raman data [44–47].

IV. THE LOWEST ADIABATIC POTENTIAL ENERGY SURFACE

The cooperative Jahn-Teller dynamics in fullerides is highly complex and has never been assessed even for the simplest, insulating compounds. The character of JT dynamics can be understood by analyzing the lowest adiabatic potential energy surface (APES) of the crystal, when all JT centers (fullerenes) are in the ground electronic state for given distortions of the lattice.

A. Static JT effect in terms of electronic vectors at C_{60} sites

The potential energy operator for A_3C_{60} is obtained by dropping the kinetic energy of phonons (we also neglect some other contributions mentioned in Sect. IIA) from the full Jahn-Teller Hamiltonian in Eq. (1):

$$\hat{U}_{\text{JT}} = \sum_{\kappa\mathbf{k}} \frac{1}{2} \omega_{\kappa\mathbf{k}}^2 Q_{\kappa\mathbf{k}}^2 + \sum_{\mathbf{n}} \left(\hat{H}_{\text{H}}^{\mathbf{n}} + \sum_{\Gamma=E,T} \sum_{\mu} V_{\mu\Gamma} \right. \\ \left. \times \sum_{\gamma \in \Gamma} q_{\mu\gamma}^{\mathbf{n}} \sum_{\alpha, \beta} \sum_{\sigma} \langle t_1\alpha | H\gamma | t_1\beta \rangle \hat{c}_{\alpha\sigma}^{\mathbf{n}\dagger} \hat{c}_{\beta\sigma}^{\mathbf{n}} \right), \quad (5)$$

where the operator of JT coupling is expressed through Clebsch-Gordan coefficients for the icosahedral group [see the discussion after Eq. (4)]. The lowest APES is obtained by diagonalizing the electronic operator in (5) corresponding to each site \mathbf{n} and considering its lowest eigenvalues in function of local JT distortions $q_{\mu\gamma}^{\mathbf{n}}$. Thus obtained function of local JT distortions of all sites of the crystal is further investigated for extremes.

For the investigation of the extremes of APES there exists a more convenient approach proposed by Öpik and Pryce for molecular JT problems [48], which we extend here. It essentially exploits the existence of a bijective relation (one-to-one correspondence) between the extremes of an APES and the electronic function corresponding to nuclear distortions in these extremes. Basing on this property, Öpik and Pryce proposed to find first the equilibrium nuclear coordinates for an arbitrary form of the electronic wave function (expressed via arbitrary fixed parameters - adiabatic coordinates), and then to investigate the extremes of the obtained energy functional in the space of these adiabatic coordinates. These adiabatic coordinates can be viewed as directional cosines of the vector representing an arbitrary wave function in the functional space of electronic basis functions involved in the Jahn-Teller effect. The representation via such vectors (electronic pseudospins) was widely used for the investigation of static JT effect in molecular systems and cooperative JT effect in solids for simple JT interaction on sites. It was extended for molecular systems with multimode vibronic coupling [49]. Here we further extend this approach over multimode JT coupling in crystals involving multielectronic JT sites, a situation realized in our fullerides.

The basis of electronic wave functions involved in JT effect at a C_{60}^{3-} ion includes spin doublet terms of the t_{1u}^3 electronic configuration, the atomic-like 2P and 2D molecular terms amounting to eight electronic wave functions for a given projection of the total spin $S = 1/2$ [50, 51]. For arbitrary distortions, in the presence of multiplet splitting operator $\hat{H}_{\text{H}}^{\mathbf{n}}$ all these eight electronic states (equivalently eight spin-doublet Slater determinants) are generally admixed to the ground adiabatic wave function of C_{60}^{3-} . However, it was shown [13] that in the case of multiply charged fullerene anions, with $n = 2, 3, 4$, the ground adiabatic multielectronic wave function corresponds in a good approximation to the lowest eigenvalue of the operator of JT coupling only. This means that the effect of multiplet splitting operator $\hat{H}_{\text{H}}^{\mathbf{n}}$ can be taken into account in the lowest order of perturbation theory. This is done in Sect. IV B.1.

Given the JT coupling at each site is described by one-electron operators, Eq. (5), its ground-state multielectronic eigenfunction ($\Psi_{\sigma}^{\mathbf{n}}$) is a Slater determinant of the lowest occupied eigenorbitals (adiabatic orbitals) $\psi_{i\sigma}^{\mathbf{n}} = \hat{a}_{i\sigma}^{\mathbf{n}\dagger} |0\rangle$, (Fig. 4(a)):

$$\Psi_{\sigma}^{\mathbf{n}} = \hat{a}_{2\sigma}^{\mathbf{n}\dagger} \hat{a}_{3\uparrow}^{\mathbf{n}\dagger} \hat{a}_{3\downarrow}^{\mathbf{n}\dagger} |0\rangle, \\ \hat{a}_{3\sigma}^{\mathbf{n}\dagger} = x_{\mathbf{n}} \hat{c}_{x\sigma}^{\mathbf{n}\dagger} + y_{\mathbf{n}} \hat{c}_{y\sigma}^{\mathbf{n}\dagger} + z_{\mathbf{n}} \hat{c}_{z\sigma}^{\mathbf{n}\dagger}, \\ \hat{a}_{2\sigma}^{\mathbf{n}\dagger} = \bar{x}_{\mathbf{n}} \hat{c}_{x\sigma}^{\mathbf{n}\dagger} + \bar{y}_{\mathbf{n}} \hat{c}_{y\sigma}^{\mathbf{n}\dagger} + \bar{z}_{\mathbf{n}} \hat{c}_{z\sigma}^{\mathbf{n}\dagger}, \quad (6)$$

where the adiabatic coordinates x, y, z and $\bar{x}, \bar{y}, \bar{z}$ are directional cosines of the doubly occupied and the half filled adiabatic orbitals (Fig. 4(a)) w.r.t. three Cartesian axes representing the reference t_{1u} orbitals (Fig. 4(b)). The unit vectors (x, y, z) and $(\bar{x}, \bar{y}, \bar{z})$ are obviously orthogonal. Due to the electronic independence of the sites, the

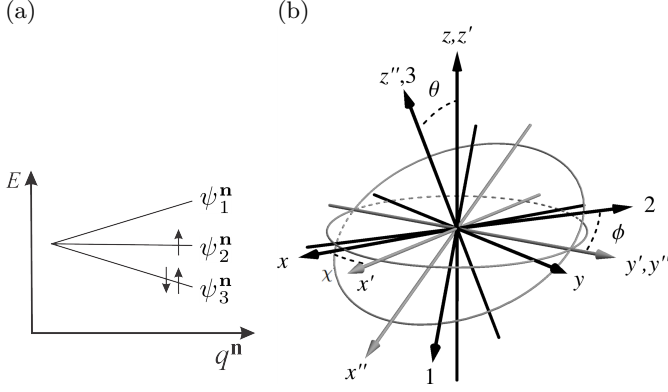


FIG. 4. Adiabatic orbitals at C_{60}^{3-} sites. (a) Splitting and population of adiabatic orbitals in the ground adiabatic electronic state $\Psi_{\uparrow}^{\mathbf{n}}$. (b) Adiabatic orbitals 1,2,3 obtained from the rotations of orthonormal LUMO orbitals x, y, z (corresponding to $t_{1u}\alpha$, $\alpha = x, y, z$) by three Euler angles.

ground-state adiabatic wave function of the whole crystal Φ is merely a direct product of adiabatic wave functions $\Psi_{\sigma}^{\mathbf{n}}$ at different sites,

$$\Phi = \prod_{\mathbf{n}} \hat{a}_{2\sigma}^{\mathbf{n}\dagger} \hat{a}_{3\uparrow}^{\mathbf{n}\dagger} \hat{a}_{3\downarrow}^{\mathbf{n}\dagger} |0\rangle. \quad (7)$$

Averaging the potential energy operator (5) on the ground-state adiabatic wave function (7), we obtain:

$$\langle U \rangle \equiv \langle \Phi | \hat{U}_{\text{JT}} | \Phi \rangle = \sum_{\kappa\mathbf{k}} \frac{1}{2} \omega_{\kappa\mathbf{k}}^2 Q_{\kappa\mathbf{k}}^2 + \sum_{\mathbf{n}} \left[\langle \Psi_{\sigma}^{\mathbf{n}} | \hat{H}_{\text{H}}^{\mathbf{n}} | \Psi_{\sigma}^{\mathbf{n}} \rangle + \sum_{\Gamma=E,T} \sum_{\mu} V_{\mu\Gamma} \sum_{\gamma \in \Gamma} q_{\mu\gamma}^{\mathbf{n}} (2R_{\gamma}^{\mathbf{n}} + \bar{R}_{\gamma}^{\mathbf{n}}) \right], \quad (8)$$

where R and \bar{R} are tensorial combinations of adiabatic coordinates:

$$\begin{aligned} R_{\gamma}^{\mathbf{n}} &= \sum_{\alpha,\beta} \langle t_1\alpha | H_{\gamma} | t_1\beta \rangle \alpha^{\mathbf{n}} \beta^{\mathbf{n}}, \\ \bar{R}_{\gamma}^{\mathbf{n}} &= \sum_{\alpha,\beta} \langle t_1\alpha | H_{\gamma} | t_1\beta \rangle \bar{\alpha}^{\mathbf{n}} \bar{\beta}^{\mathbf{n}}. \end{aligned} \quad (9)$$

Next we minimize the expression (8) w.r.t. nuclear coordinates. Having in mind that the phonon coordinates form a complete, linearly independent set, we first expand the local JT distortions on sites through the latter (the Van Vleck expansion):

$$q_{\mu\gamma}^{\mathbf{n}} = \sum_{\kappa\mathbf{k}} a_{\mu\gamma}^{\mathbf{n}}(\kappa\mathbf{k}) Q_{\kappa\mathbf{k}}, \quad (10)$$

where $a_{\mu\gamma}^{\mathbf{n}}(\kappa\mathbf{k})$ are Van Vleck coefficients [52]. They are obtained by decomposition of $q_{\mu\gamma}^{\mathbf{n}}$ into the displacements of involved atoms, and the latter into phonon coordinates using the calculated phonon frequencies and polarization

vectors in Sect III. Substituting (10) into (8) and minimizing the obtained expression after phonon coordinates, we obtain the equilibrium value of the latter,

$$Q_{\kappa\mathbf{k}}^{(0)} = -\frac{1}{\omega_{\kappa\mathbf{k}}^2} \sum_{\mathbf{n}} \sum_{\Gamma=E,T} \sum_{\mu} V_{\mu\Gamma} \sum_{\gamma \in \Gamma} a_{\mu\gamma}^{\mathbf{n}}(\kappa\mathbf{k}) (2R_{\gamma}^{\mathbf{n}} + \bar{R}_{\gamma}^{\mathbf{n}}), \quad (11)$$

in terms of adiabatic coordinates on sites. Substituting the equilibrium coordinates (11) back into the potential energy expression (8) we obtain its equilibrium (extremal after $Q_{\kappa\mathbf{k}}$) form in terms of adiabatic coordinates only:

$$\begin{aligned} \langle U \rangle^{(0)} &= \sum_{\mathbf{n}} \langle \Psi_{\sigma}^{\mathbf{n}} | \hat{H}_{\text{H}}^{\mathbf{n}} | \Psi_{\sigma}^{\mathbf{n}} \rangle - \frac{1}{2} \sum_{\mathbf{n}_1} \sum_{\mathbf{n}_2} \sum_{\mu_1\Gamma_1} \sum_{\mu_2\Gamma_2} V_{\mu_1\Gamma_1} V_{\mu_2\Gamma_2} \\ &\times \sum_{\gamma_1 \in \Gamma_1} \sum_{\gamma_2 \in \Gamma_2} \zeta_{\mu_1\gamma_1}^{\mu_2\gamma_2}(\mathbf{n}_2 - \mathbf{n}_1) \\ &\times (2R_{\gamma_1}^{\mathbf{n}_1} + \bar{R}_{\gamma_1}^{\mathbf{n}_1}) (2R_{\gamma_2}^{\mathbf{n}_2} + \bar{R}_{\gamma_2}^{\mathbf{n}_2}), \end{aligned} \quad (12)$$

where the introduced parameters,

$$\zeta_{\mu_1\gamma_1}^{\mu_2\gamma_2}(\mathbf{n}_2 - \mathbf{n}_1) = \sum_{\kappa\mathbf{k}} \frac{a_{\mu_1\gamma_1}^{\mathbf{n}_1}(\kappa\mathbf{k}) a_{\mu_2\gamma_2}^{\mathbf{n}_2}(\kappa\mathbf{k})}{\omega_{\kappa\mathbf{k}}^2}, \quad (13)$$

describe the relaxation of the lattice along the local nuclear coordinates $q_{\mu_1\gamma_1}^{\mathbf{n}_1}$ in response to local JT distortions $q_{\mu_2\gamma_2}^{\mathbf{n}_2}$ of unity amplitude. Due to translation symmetry of fullerene sites, these parameters depend only on the lattice vector connecting the positions of two local distortions. It is evident from Eqs. (13) and (10), that the knowledge of the phonon polarization vectors and frequencies allows to define completely these parameters.

The tensors R_{γ} are obtained from Eq. (9) using explicit JT matrices in (4):

$$\Gamma = E :$$

$$R_{\theta} = \frac{1}{2}(x^2 + y^2) - z^2, \quad R_{\epsilon} = -\frac{\sqrt{3}}{2}(x^2 - y^2),$$

$$\Gamma = T :$$

$$R_{\xi} = \sqrt{3}yz, \quad R_{\eta} = \sqrt{3}xz, \quad R_{\zeta} = \sqrt{3}xy, \quad (14)$$

and similar expressions (in terms of \bar{x} , \bar{y} and \bar{z}) hold for tensors \bar{R}_{γ} (we dropped for simplicity all indices \mathbf{n}).

It is convenient to present the APES from Eq. (12) as a sum of one-site and two-sites contributions,

$$\langle U \rangle^{(0)} = \sum_{\mathbf{n}} W_{\mathbf{n}}^{(1)} + \sum_{\mathbf{n}_1 < \mathbf{n}_2} W_{\mathbf{n}_1, \mathbf{n}_2}^{(2)}. \quad (15)$$

where $W^{(1)}$ and $W^{(2)}$ depend on the adiabatic coordinates of one center and two centers, respectively. In the following we calculate and analyze these quantities for different A_3C_{60} .

B. APES at individual JT sites

The contributions $W_{\mathbf{n}}^{(1)}$ (terms $\mathbf{n}_1 = \mathbf{n}_2$ in (12)) involve response parameters (13) obeying the following relations

[53]:

$$\zeta_{\mu_1\gamma_1}^{\mu_2\gamma_2}(\mathbf{0}) = \zeta_{\mu_1\gamma_1}^{\mu_2\gamma_1}(\mathbf{0})\delta_{\gamma_1,\gamma_2} \equiv \zeta_{\mu_1\mu_2}^\Gamma \delta_{\gamma_1,\gamma_2}, \quad (16)$$

where $\zeta_{\mu_1\mu_2}^\Gamma$ is common for all $\gamma \in \Gamma$. Then the contribution to the APES from a given JT site can be written as follows (we drop hereafter the index of the site):

$$W^{(1)} = \langle |\Psi_\sigma| \hat{H}_H |\Psi_\sigma\rangle - \frac{1}{2} \sum_{\Gamma=E,T} \left[\sum_{\mu_1\mu_2} V_{\mu_1\Gamma} V_{\mu_2\Gamma} \zeta_{\mu_1\mu_2}^\Gamma \right] \times \sum_{\gamma \in \Gamma} (2R_\gamma + \bar{R}_\gamma)^2. \quad (17)$$

The first term is the averaged multiplet splitting interaction in the adiabatic electronic state Ψ_σ . Given the adiabatic orbitals can be seen as rotated reference electronic orbitals (Fig. 4(b)) in virtue of $t_{1u} - p$ isomorphism, the operator \hat{H}_H , being invariant under rotations of coordinate system, could be written in the basis of adiabatic orbitals from the beginning. That is the $\hat{c}_{\alpha\sigma}$, ($\alpha = x, y, z$) operators in Eq. (3) can be replaced by the $\hat{a}_{i\sigma}$ ($i = 1, 2, 3$) operators, Eq. (6) (the lacking operator $\hat{a}_{1\sigma}$ is uniquely defined for given $\hat{a}_{2\sigma}$ and $\hat{a}_{3\sigma}$). Therefore, the matrix element of \hat{H}_H will not depend on the adiabatic coordinates, i.e., will be a constant,

$$\langle \Psi_\sigma | \hat{H}_H | \Psi_\sigma \rangle = E_H, \quad (18)$$

linearly scaling with J_H .

The JT part in (17) can be conveniently rewritten as follows. Consider first equal quantities in the square brackets for both Γ . Then the last summation in (17) can be extended over all $\gamma \in H$ which, after substituting Eqs. (14), gives the following equalities:

$$\begin{aligned} \sum_{\gamma \in H} R_\gamma^2 &= \sum_{\gamma \in H} \bar{R}_\gamma^2 = 1, \\ \sum_{\gamma \in H} R_\gamma \bar{R}_\gamma &= -1/2. \end{aligned} \quad (19)$$

The second relation becomes evident if one passes to a coordinate system XYZ where one adiabatic vector (x, y, z) is directed along Z and the other, $(\bar{x}, \bar{y}, \bar{z})$, lies in the XY plane. The obtained relations show that the one-site APES is independent from electronic coordinates in the considered case. Given that the latter are parameterized by three Euler angles (Fig. 4(b)), we conclude that a three-dimensional continuum of equipotential minima (a three-dimensional trough) is realized at the bottom of lowest APES in this approximation. The motion at the bottom of this trough is isomorphic with the rotation of a rigid body which determines the structure of low-lying vibronic levels in isolated C_{60}^{3-} ions [50, 51].

Using the relations (19), Eq. (17) can be given in two equivalent forms:

$$W^{(1)} = E_H - 3E_{JT}^E + (E_{JT}^E - E_{JT}^T) \sum_{\gamma \in T} (2R_\gamma + \bar{R}_\gamma)^2, \quad (20)$$

or

$$W^{(1)} = E_H - 3E_{JT}^T + (E_{JT}^T - E_{JT}^E) \sum_{\gamma \in E} (2R_\gamma + \bar{R}_\gamma)^2, \quad (21)$$

where the parameters

$$\begin{aligned} E_{JT}^E &= \frac{1}{2} \sum_{\mu_1\mu_2} V_{\mu_1 E} V_{\mu_2 E} \zeta_{\mu_1\mu_2}^E, \\ E_{JT}^T &= \frac{1}{2} \sum_{\mu_1\mu_2} V_{\mu_1 T} V_{\mu_2 T} \zeta_{\mu_1\mu_2}^T, \end{aligned} \quad (22)$$

are JT stabilization energies after the distortions of E and T type, respectively, in the case of a single electron presenting in the t_{1u} shell. The last term in (20) and (21) describes the warping of the bottom of the trough in terms of adiabatic coordinates of two occupied adiabatic orbitals (equivalently three Euler angles). The parameter defining the amplitude of the warping scales with the difference of energies of JT stabilization after the distortions of E and T type. When these two stabilization energies are equal, the warping contribution disappears and we end up with a three-dimensional trough similarly to an isolated C_{60}^{3-} ion. Given the complexity of the systems (multicenter and multimode JT effect) the expression for $W^{(1)}$ looks remarkably simple. In the following we analyze the contributions to $W^{(1)}$ in different cubic fullerides using the calculated vibronic constants and phonon spectra.

1. Contributions to the static JT stabilization

A consistent definition of JT stabilization energy in the presence of warping is obtained via averaging the second term in Eq. (17) over all points of the trough. This is equivalent with the averaging over adiabatic coordinates (Euler angles) of the sums involving R_γ and \bar{R}_γ for $\gamma \in E$ and $\gamma \in T$, respectively. Integration over all Euler angles gives for these terms the weights $2/5$ and $3/5$, respectively. With them we can write for the Jahn-Teller stabilization energy,

$$E_{JT} = 3 \left(\frac{2}{5} E_{JT}^E + \frac{3}{5} E_{JT}^T \right). \quad (23)$$

In the limit of an isolated C_{60}^{3-} , when the coupling to the vibrational eigenmodes is considered from the beginning, the Van Vleck coefficients in Eq. (10) become elements of a unity matrix, so that the response matrix ζ becomes diagonal too, $\zeta_{\mu_1\mu_2}^H = \delta_{\mu_1,\mu_2}/\omega_{\mu H}^2$. Then we recover the usual expression for the multimode $t \otimes H$ JT problem involving three electrons, $E_{JT} = (3/2) \sum_{\mu} V_{\mu H}^2/\omega_{\mu H}^2$.

The first term in (17) can be evaluated more accurately than suggested in Eq. (24), by applying a second order perturbation theory after \hat{H}_H (see the SM [33]), yielding

$$E_H^{(2)} = J_H - \frac{J_H^2}{4E_{JT}} \quad (24)$$

TABLE IV. The JT stabilization energy and its contributions (in meV). The JT stabilization energy of isolated C_{60}^{3-} is -150.9 meV.

	fcc						A15	
	K_3C_{60}		Rb_3C_{60}		Cs_3C_{60}		Cs_3C_{60}	
	LDA	PBE	LDA	PBE	LDA	PBE	LDA	PBE
F^a	-144.9	-153.6	-148.9	-153.4	-150.1	-155.3	-150.4	-156.7
	-171.1	-179.5	-176.7	-181.7	-184.6	-190.4	-178.0	-187.3
A^a	-16.1	-7.2	-17.6	-2.5	-19.0	-3.9	-3.0	-2.7
	-15.7	-6.8	-17.3	-2.4	-18.7	-3.9	-3.0	-2.7
FF^a	-0.2	-0.2	-0.2	-0.1	-0.2	-0.1	-0.2	-0.1
	-0.1	-0.1	-0.1	-0.1	-0.1	-0.1	-0.2	-0.1
A-F	-0.2	-0.2	-0.4	-0.1	-0.6	-0.2	0.6	0.7
F-FF	0.0	0.0	0.0	0.0	0.1	0.1	0.0	-0.0
A-FF	-0.0	-0.1	-0.0	-0.0	-0.0	-0.0	0.0	0.0
E_{JT}	-161.4	-161.2	-167.1	-156.1	-169.8	-159.5	-152.9	-158.8

^aThe data in the second row correspond to the neglect of off-diagonal contributions after μ .

The first term here is the destabilization energy [the only one given by Eq. (24)], while the second term represents a small correction due to a small value of Hund's coupling parameter (ca 40 meV) compared to the E_{JT} of ca 150 meV [54, 55]. Note that the stabilization energy is further increased in C_{60}^{3-} by ca 90 meV due to a dynamical delocalization of JT distortions in the trough [54, 55], which diminishes further this correction thus enhancing the criterion of applicability of single-determinant adiabatic wave function (6). In the following we neglect the contribution (24) which only gives a constant shift of energy on sites.

This elastic response parameters $\zeta_{\mu_1\mu_2}^\Gamma$ can be expressed through the lattice Green's functions [53, 56]. Evaluating the latter via the integration over the Brillouin zone of the crystal for atomic displacements of different pairs of atoms we obtain the elastic response parameters for all relevant local modes and evaluate their contribution to E_{JT} .

Table IV shows the calculated E_{JT} as well as its contributions from different modes. The components F, A and FF are separated contributions from intrafullerene, alkali and interfullerene modes, respectively. We can see that the off-diagonal contributions after μ (the interference terms) are important for intrafullerene H_g modes because the latter are not vibrational eigenmodes in fullerenes. The next rows, A-F, F-FF and A-FF, represent the contributions from alkali-intrafullerene, intrafullerene-interfullerene and interfullerene-alkali interference terms. We may conclude that the intrafullerene modes give the major contribution to JT stabilization as expected, while interaction with alkali mode increases E_{JT} by few percents in LDA calculations. At the same time the effect of interfullerene modes is negligible.

To get further insight into the origin of these contributions we inspect the elastic response parameters en-

tering Eqs. (22), which have the meaning of inverse effective force constants (rigidity) w.r.t. the corresponding active distortion mode. The inverse square root of $\zeta_{\mu\mu}^\Gamma$ which corresponds to the effective frequency of the corresponding mode can be referred in SM [33]. We can see that in the case of intrafullerene modes these agree well with the corresponding vibrational eigenmodes of isolated fullerene ion supporting the molecular crystal character of fullerenes. At the same time, the effective frequencies for alkali and interfullerene modes are much lower amounting to few tens of wave numbers for some of them. This explains the obtained important contribution of alkali modes to the JT stabilization despite the vibronic coupling constants are one order of magnitude smaller than for intrafullerene modes. Partly the small value of $(\zeta_{\mu\mu}^\Gamma)^{-1/2}$ for alkali modes is explained by the existence of low-frequency optical phonons involving these modes as it is evident from the phonon dispersion (Fig. 3). Another contribution comes from the acoustic phonons as can be seen from Table VIII.

2. Warping of the APES

Weighting the expressions (20) and (21) in a similar way as in Eq. (23), we obtain:

$$W^{(1)} = E_H - E_{JT} + W_{\text{warp}}, \quad (25)$$

where the warping term is given by

$$W_{\text{warp}} = \frac{1}{2}(E_{JT}^E - E_{JT}^T) \left[\frac{2}{5} \sum_{\gamma \in T} (2R_\gamma + \bar{R}_\gamma)^2 - \frac{3}{5} \sum_{\gamma \in E} (2R_\gamma + \bar{R}_\gamma)^2 \right]. \quad (26)$$

Note that the warping term now averages to zero when integrated over the trough.

Using the equality

$$\sum_{\gamma \in H} (2R_\gamma - \bar{R}_\gamma)^2 = 3, \quad (27)$$

emerging from the relations (19), we can represent the warping term (26) only in terms of tensors with $\gamma \in T$ only:

$$W_{\text{warp}} = \Delta \left[-\frac{9}{5} + \sum_{\gamma \in T} (2R_\gamma + \bar{R}_\gamma)^2 \right], \quad (28)$$

where the warping parameter was introduced:

$$\Delta = \frac{1}{2}(E_{JT}^E - E_{JT}^T) \quad (29)$$

This parameter is evaluated in a similar way as E_{JT} . Table V gives the calculated Δ for the four materials, as well as its separated contributions from intrafullerene, alkali

and interfullerene modes and their interference. The notations and meaning of the columns are similar to Table IV. We observe that the main contribution to the warping comes almost entirely from alkali modes in the case of fcc fullerides and from the intrafullerene modes in the case of A15 structure. In all compounds (except for potassium fulleride within LDA approximation) the contributions from intrafullerene and alkali atoms are of opposite sign. Note that now the interference of intrafullerene and alkali modes is relatively large. Table IX shows that Δ is mostly contributed by the acoustic phonon modes in the case of fcc fullerides. On the contrary, it is contributed by optical phonon modes in the case of A15 fulleride. We stress that the warping is entirely due to the interaction of fullerene molecules with the environment. In the case of isolated fullerene ions the warping of the lowest APES doesn't arise in the approximation of linear JT coupling. On the other hand, the quadratic JT coupling was shown to have negligible effect on its warping [32].

The warping itself arises from the second factor in (28). This factor represents a warping function which depends on the adiabatic coordinates only and is universal for all investigated fullerides. For the sake of analysis, consider first the case of only two electrons in the lowest adiabatic orbital (the case of C_{60}^{2-} ion). In the absence of warping this situation leads to a two-dimensional trough in the space of spherical angles θ and ϕ because of the constraint $x^2 + y^2 + z^2 = 1$. The warping function reduces in this case to an expression depending only on the adiabatic coordinates of this adiabatic orbital, $-6[x^4 + y^4 + z^4 - (7/10)r^4]$, where $r = 1$. The expression in the square brackets coincides up to a constant $-1/10$ with the fourth-order cubic invariant [57]. Such a function was considered phenomenologically by O'Brien in connection with the warping of the lowest APES of $d \otimes H$ JT problem [22, 51] subject to a perturbation from a cubic environment. The obtained warping function is shown in Fig. 5a and has similar extremal properties as in the case of $d \otimes H$ JT problem. Thus two groups of extremes, three of [001] type (tetragonal) and four of [111] type (trigonal) appear, which are either minima or maxima depending on the sign of the parameter Δ . On the contrary, six extremes of [011] type (rhombic) are always saddle points.

In the case of C_{60}^{3-} , the warping function will depend on three additional adiabatic coordinates entering the tensors \bar{R}_γ in (28). It is easier, therefore, to investigate it in the space of three Euler angles defining both occupied adiabatic orbitals (Fig.5b). To this end we need to express the six adiabatic coordinates entering Eq. (28) via these angles [50, 51],

$$\begin{aligned} x &= \sin \theta \cos \phi, & y &= \sin \theta \sin \phi, & z &= \cos \theta, \\ \bar{x} &= -\sin \chi \cos \theta \cos \phi - \cos \chi \sin \phi, \\ \bar{y} &= \cos \chi \cos \phi - \sin \chi \cos \theta \sin \phi, \\ \bar{z} &= \sin \chi \sin \theta. \end{aligned} \quad (30)$$

The obtained $\theta - \phi$ maps of the warping function for several values of the angle χ are shown in Fig. 5b. We

can see that the extremal structure of the lowest APES has the same morphology as in the case of C_{60}^{2-} (Fig. 5a). The new feature is the cyclic shift of the landscape in function of χ with a period of π . For $\Delta > 0$ the minima are of trigonal type and the lowest energy path connecting pairs of these minima, e.g., [111] and [1-11] (not shown in Fig. 5), is via the saddle points ([101]). For $\Delta < 0$ the minima are of tetragonal type (e.g., [001]) and the lowest-energy path connecting minima of these type are again saddle points albeit now the path passes through them in a perpendicular direction.

To establish the character of JT dynamics, it is necessary to know the height of the barrier (the energy of the saddle point measured from the minimum) separating the minima. Fig. 6a shows the dependence of the barriers on the angle χ . One can see that the barrier doesn't depend on χ in the case of trigonal minima, whereas its height oscillates periodically in the case of tetragonal minima. In all systems and for all χ the height of the barrier is smaller than 4 meV which, at its turn, is smaller than the rotational quantum in the trough for an isolated C_{60}^{3-} (ca 8 meV) and much smaller than the kinetic delocalization energy of JT deformations in this anion (ca 90 meV) [54, 55]. This precludes the localization JT deformation after θ and ϕ in vicinity of the minima. At the same time, the energy of the minima is independent from χ irrespective of their type (Fig. 6b). This means that a one-dimensional trough after the coordinate $0 < \chi \leq 2\pi$ will be preserved for the warping of any amplitude, a situation not realized in the case of the cubic warping of a two-dimensional trough as Fig. 5a shows.

On the basis of these results we conclude that the JT dynamics at one site in the A_3C_{60} cubic fullerides corresponds to weakly hindered rotations of JT deformations in the three-dimensional trough.

C. Intersite interaction of JT centers

The two-site contributions to the lowest APES, $W_{\mathbf{n}_1, \mathbf{n}_2}^{(2)}$, can be extracted from Eq. (12) in the following form:

$$\begin{aligned} W_{\mathbf{n}_1, \mathbf{n}_2}^{(2)} &= \sum_{\Gamma_1} \sum_{\Gamma_2} \sum_{\gamma_1 \in \Gamma_1} \sum_{\gamma_2 \in \Gamma_2} B_{\gamma_1}^{\gamma_2}(\mathbf{n}_2 - \mathbf{n}_1) \\ &\quad \times (2R_{\gamma_1}^{\mathbf{n}_1} + \bar{R}_{\gamma_1}^{\mathbf{n}_1})(2R_{\gamma_2}^{\mathbf{n}_2} + \bar{R}_{\gamma_2}^{\mathbf{n}_2}), \\ B_{\gamma_1}^{\gamma_2}(\mathbf{n}_2 - \mathbf{n}_1) &\equiv -\frac{1}{2} \sum_{\mu_1 \in \Gamma_1} \sum_{\mu_2 \in \Gamma_2} V_{\mu_1 \Gamma_1} V_{\mu_2 \Gamma_2} \\ &\quad \times \zeta_{\mu_1 \gamma_1}^{\mu_2 \gamma_2}(\mathbf{n}_2 - \mathbf{n}_1). \end{aligned} \quad (31)$$

We calculated the interaction parameters $B_{\gamma_1}^{\gamma_2}(\Delta \mathbf{n})$ for nearest neighbor and next nearest neighbor fullerene pairs. In the former case $\Delta \mathbf{n} \parallel [101]$ for fcc and $\parallel [111]$ for bcc fullerides, respectively (Fig. 1). The next nearest neighbors are located along cubic axes for both kind of lattices ($\Delta \mathbf{n} \parallel [001]$). The results are given in Tables VII and IX.

TABLE V. The warping parameter Δ and its contributions (in meV).

	fcc						A15	
	K ₃ C ₆₀		Rb ₃ C ₆₀		Cs ₃ C ₆₀		Cs ₃ C ₆₀	
	LDA	PBE	LDA	PBE	LDA	PBE	LDA	PBE
F ^a	0.044	-0.526	-0.577	-1.109	-1.112	-1.809	-0.532	-0.287
	1.992	1.670	1.715	1.104	1.798	0.706	0.150	0.485
A ^a	4.454	1.548	4.727	0.402	4.869	0.668	0.137	0.211
	4.362	1.464	4.670	0.380	4.825	0.643	0.340	0.371
FF ^a	-0.018	-0.014	-0.019	-0.015	-0.025	-0.017	-0.003	-0.006
	-0.014	-0.009	-0.015	-0.011	-0.018	-0.011	0.003	0.000
A-F	0.153	0.194	0.256	0.148	0.333	0.213	-0.179	-0.123
F-FF	-0.036	-0.060	-0.043	-0.032	-0.065	-0.052	-0.003	0.003
A-FF	0.021	0.023	0.019	0.009	0.020	0.010	-0.024	-0.017
Δ	4.618	1.165	4.364	-0.598	4.019	-0.985	-0.605	-0.220

^aThe data in the second row correspond to the neglect of off-diagonal contributions after μ .

One can see that the interaction parameters for the A15 fulleride are much smaller than in fcc compounds. A similar situation was also found for the warping parameter (Table VII) pointing to a generally weaker symmetry lowering effect in bcc lattices compared to fcc ones (we remind that in the present calculations the merohedral order in the A15 compound was replaced by a full order of fullerene molecules). In fcc fullerenes the interaction parameters corresponding to different pairs $\gamma_1\gamma_2$ is highly selective. Actually, it is non-negligible only for $\theta\theta$, $\theta\xi$ and $\xi\xi$ coupling in nearest neighbors and only for $\theta\theta$ coupling in next nearest neighbor pairs. Remarkably, the latter is significantly stronger than all coupling in the nearest neighbor pairs. Even so it doesn't exceed 4 meV (LDA result for Cs₃C₆₀). However, the interaction with more distant fullerenes is negligible. We expect that the interaction of these pairs is mainly governed by acoustic phonon modes due to their larger dispersion (Fig. 2), which implies its R^{-3} dependence on the interfullerene separation R .

We may conclude from this study that the interaction of JT distortions on different fullerene sites is too weak to quench their dynamics and localize them at some points in the troughs. There can be however some correlation in the rotations of these distortions. For instance, for the strongest $\theta\theta$ coupling of next nearest neighbor pairs the maximal negative value of the corresponding tensorial factor in Eq. (31) reaches -9/4 for θ distortions on the two sites of opposite sign. For fcc Cs₃C₆₀ this gives a correlation energy amounting to half of rotational quantum (in the LDA calculation). We can speculate that this interaction can give rise at low temperature to an antiferrodistorsive ordering of θ distortions at next nearest neighbor fullerene sites. These static distortions are expected to have a small amplitude and will coexist with the rotation of JT deformations of much larger amplitude at each C₆₀. This scenario corroborate the low-temperature NMR data for insulating fcc Cs₃C₆₀ which

evidence weak static distortions of fullerenes gradually disappearing with the rise of temperature [19].

Finally we would like to point out that the results of the present and previous subsections are strongly dependent on the type of exchange correlation functional used in the DFT calculations. While it is not clear for the moment what functional from the two employed here is to be preferred for phonon calculations (there is no clear answer from the literature), we notice that the use of more involved hybrid functionals is prohibited for the present systems due to a large number of atoms in the unit cell (even for the highest degree of ordering of fullerene molecules in the lattice). To unambiguously determine the low-energy phonon dispersion, it is desired that such calculations will become feasible.

V. DISCUSSION AND CONCLUSIONS

In this paper, we investigate for the first time the modification of JT effect on fullerene anions C₆₀³⁻ when they are incorporated in the cubic lattices of A₃C₆₀ fullerenes. The interaction of each fullerene molecule with the environment leads to modification of JT stabilization energy and to the warping of the trough at each fullerene site, as well as to the interaction of JT distortions at different sites. We studied these effects in three fcc fullerenes with A=K,Rb,Cs and in Cs₃C₆₀ with bcc (A15) structure by using the results of DFT calculations of orbital vibronic coupling constants at C₆₀ sites and of phonon spectra of these materials. The key quantities defining the character of JT effect in these crystals are the elastic response parameters for local JT distortions, which are evaluated on the basis of phonon calculations. Using these response parameters and the vibronic coupling constants the lowest APES has been calculated and analyzed in these materials. To this end, an expression for the lowest APES in function of trough coordinates at the fullerene sites has

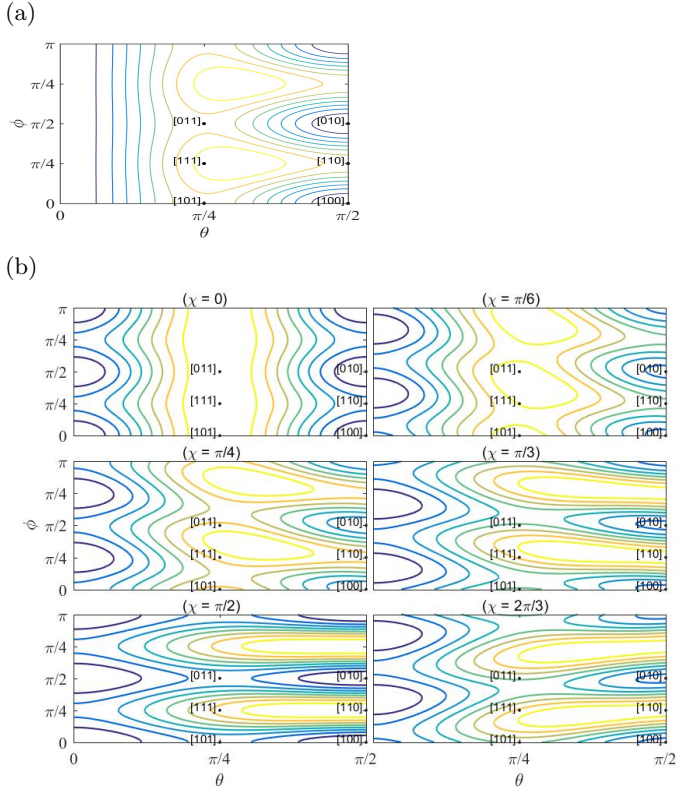


FIG. 5. Contour plots of the warping function in Eq. (28) for an irreducible domain of Euler angles θ and ϕ (a) C_{60}^{2-} ion with cubic warping. (b) Cross section of a three-dimensional surface, corresponding to the APES of C_{60}^{3-} site in cubic A_3C_{60} , at indicated values of Euler angle χ . The lines correspond to increasing energies for colors varying from white to black.

been derived. We found that the JT stabilization energy increases by few percents compared to isolated C_{60}^{3-} and a warping of the trough amounting to few meV occurs in all investigated compounds. The interaction of JT distortions on nearest- and next-nearest-neighbor fullerene sites is quite selective w.r.t. to their symmetry and turns out to be of similar order of magnitude as the warping of the APES on individual sites. All these effects are mostly due to the interaction of C_{60} ions with the displacements of neighbor alkali atoms.

The obtained results concerning the APES of A_3C_{60} are sufficient for the description of eventual static cooperative JT effect in such systems, i.e., the distorted equilibrium geometry and its evolution with the temperature, including the structural phase transition [20, 58]. However, in cubic fullerides the dynamical JT effect on fullerene sites, destroying any ordering of static JT deformations is the most probable scenario [13, 59] because the energy of kinetic delocalization of JT deformations along the trough is of the order of ca 90 meV [54], which exceeds by two orders of magnitude the interaction parameters for JT active distortions on nearest-neighbor fullerene sites (Table VI). Given this situation, the dy-

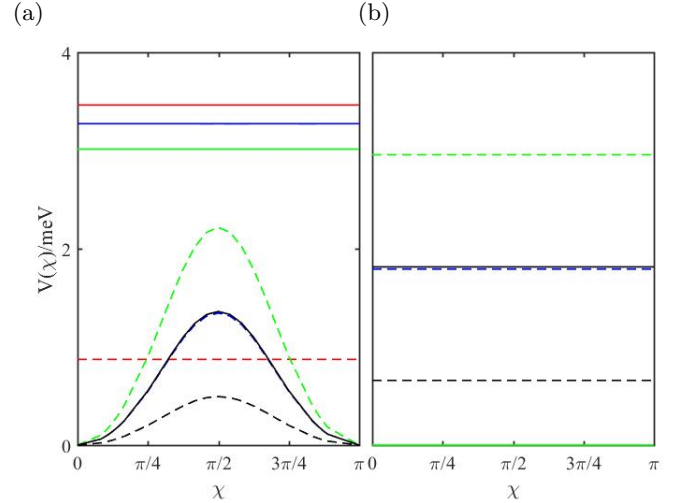


FIG. 6. Calculated barriers (a) and energies of the minimum (b) of the lowest APES at a C_{60}^{3-} in cubic fullerides in function of the Euler angle χ . The energy of the lowest minimum among the investigated systems is taken as zero in (b). Solid and dashed lines are the results of LDA and PBE calculations; red, blue, green, and black lines correspond to fcc K_3C_{60} , Rb_3C_{60} , Cs_3C_{60} and $A15 Cs_3C_{60}$ fullerides. In (b), the solid red and blue lines are hidden behind the solid green line; the dashed red line is hidden behind the solid green line.

namical cooperative JT effect could be considered within an approach using a single set of H_g modes (effective modes) on each fullerene site [13, 54] with JT, warping and interaction parameters derived in the present work. One should note, however, that the latter will be further modified when the JT dynamics on sites is considered in a pretty similar way as the isotope substitution leads to localization of JT distortions in perfectly equipotential troughs [60]. However, such modifications are not expected to change the order of magnitude of the calculated parameters corresponding to static JT distortions. We may conclude, therefore, that the present study supports the picture of weakly hindered independent rotations of JT deformations at C_{60} sites in all A_3C_{60} .

The results obtained in this work are relevant to a number of the observable properties of insulating cubic fullerides such as the NMR [19] and infrared [17, 18] spectra. For instance, a weak localization of JT distortions on fullerene sites due to their elastic coupling could slightly lower the symmetry of C_{60} anions, which can be the reason for the “orbital glass” behavior found in the NMR spectra of Cs_3C_{60} [19]. This static and dynamic symmetry lowering of fullerene molecules is also expected to show up in the fine structure of infrared spectra of insulating A_3C_{60} , the reason for which the latter have not been completely assigned by the simulations of isolated C_{60}^{3-} units [61]. Complementary information on the JT dynamics is expected to be gained from other spectroscopy as well such as optical absorption, Raman and

TABLE VI. The interaction parameter $B_{\gamma_1}^{\gamma_2}(\Delta\mathbf{n})$ for nearest neighbor fullerene sites (in meV), calculated by LDA and PBE (parentheses).

	fcc			A15
	K ₃ C ₆₀	Rb ₃ C ₆₀	Cs ₃ C ₆₀	Cs ₃ C ₆₀
E_θ	-0.55(-0.17)	-0.52(-0.44)	-0.36(-0.39)	-0.01(-0.02)
E_ϵ	-0.06(0.09)	-0.03(0.02)	-0.02(0.01)	0.15(0.18)
E_θ T _ξ	-0.24(-0.30)	-0.26(-0.22)	-0.26(-0.24)	0.02(0.03)
T _η	0.02(0.04)	0.03(0.01)	0.03(0.02)	0.30(0.27)
T _ζ	-0.01(0.07)	-0.01(0.01)	-0.02(0.01)	-0.08(-0.13)
E_ϵ	-0.06(0.09)	-0.03(0.02)	-0.02(0.01)	0.15(0.18)
E_ϵ T _ξ	-0.06(-0.11)	-0.06(-0.04)	-0.03(-0.04)	0.01(0.01)
T _η	-0.02(-0.04)	-0.03(-0.01)	-0.03(-0.02)	-0.06(-0.09)
T _ζ	-0.03(-0.09)	-0.03(-0.01)	-0.05(-0.01)	-0.05(-0.05)
T _ξ	-0.50(-0.56)	-0.65(-0.41)	-1.04(-0.73)	0.02(-0.00)
T _η T _ξ	0.10(0.12)	0.13(0.12)	0.15(0.15)	-0.07(-0.05)
T _ζ	-0.00(0.02)	0.01(0.06)	0.00(0.04)	-0.06(-0.04)
T _η T _η	-0.07(-0.10)	-0.09(-0.08)	-0.10(-0.10)	-0.18(-0.14)
T _ζ	-0.01(0.05)	-0.01(-0.00)	-0.01(0.01)	-0.01(0.01)
T _ζ T _ζ	-0.11(0.08)	-0.05(-0.09)	0.06(-0.06)	-0.15(-0.09)

TABLE VII. The interaction parameter $B_{\gamma_1}^{\gamma_2}(\Delta\mathbf{n})$ for next nearest neighbor fullerene sites (in meV), calculated by LDA and PBE (parentheses).

	fcc			A15
	K ₃ C ₆₀	Rb ₃ C ₆₀	Cs ₃ C ₆₀	Cs ₃ C ₆₀
E_θ	2.49(0.79)	3.25(0.50)	4.20(1.07)	0.04(0.04)
E_ϵ	0.03(0.07)	0.17(0.05)	0.35(0.12)	0.00(0.02)
E_θ T _ξ	-0.00(-0.00)	-0.00(-0.00)	-0.00(-0.00)	0.03(0.05)
T _η	-0.04(-0.04)	-0.04(-0.01)	-0.06(-0.01)	0.03(0.06)
T _ζ	0.00(0.00)	0.00(0.00)	-0.00(-0.00)	0.01(0.02)
E_ϵ	0.03(0.07)	0.17(0.05)	0.35(0.12)	0.00(0.02)
E_ϵ T _ξ	0.00(0.00)	0.00(0.00)	0.00(0.00)	0.01(0.00)
T _η	-0.05(-0.08)	-0.05(-0.00)	-0.08(-0.01)	0.02(0.02)
T _ζ	-0.00(-0.00)	-0.00(-0.00)	-0.00(-0.00)	0.02(0.05)
T _ξ	-0.02(0.08)	0.04(-0.05)	0.10(-0.00)	-0.09(-0.07)
T _η T _ξ	-0.00(-0.01)	-0.01(-0.00)	-0.02(-0.01)	-0.05(-0.03)
T _ζ	0.05(0.05)	0.00(-0.01)	-0.01(-0.03)	-0.08(-0.07)
T _η T _η	0.03(0.03)	0.04(0.02)	0.03(0.03)	-0.02(-0.02)
T _ζ	0.00(0.00)	0.00(0.00)	0.00(0.00)	-0.03(-0.02)
T _ζ T _ζ	-0.02(0.01)	0.00(-0.02)	0.02(-0.03)	0.03(0.04)

inelastic neutron scattering. Further application of the present results to the rationalization of various spectroscopic data of insulating fullerenes will result in a thorough understanding of the physics of dynamical cooperative JT effect in these materials.

TABLE VIII. The contribution of acoustic modes to the total JT stabilization energy and its components (in meV).

	K ₃ C ₆₀		Rb ₃ C ₆₀		Cs ₃ C ₆₀		A15	
	LDA	PBE	LDA	PBE	LDA	PBE	LDA	PBE
F ^a	-0.1	-0.1	-0.4	-0.1	-0.8	-0.4	-0.0	-0.0
	-1.4	-0.2	-2.5	-0.1	-4.2	-0.6	-0.1	-0.3
A ^a	-12.6	-2.4	-16.5	-0.4	-18.3	-2.3	-1.0	-1.2
	-12.1	-2.3	-16.1	-0.4	-17.9	-2.3	-1.0	-1.3
FF ^a	-0.1	-0.1	-0.0	-0.1	-0.0	-0.1	-0.1	-0.1
	-0.1	-0.1	-0.0	-0.1	-0.0	-0.1	-0.1	-0.1
A-F	-0.1	-0.0	-0.4	-0.0	-0.5	-0.0	0.0	0.0
F-FF	0.0	0.1	0.1	0.0	0.1	0.1	0.0	0.0
A-FF	-0.0	-0.0	-0.0	-0.0	-0.0	-0.0	-0.0	-0.0
ΔE_{JT}	-12.9	-2.6	-17.3	-0.5	-19.6	-2.8	-1.1	-1.4

^aThe data in the second row correspond to the neglect of off-diagonal contributions after μ .

ACKNOWLEDGEMENTS

Z.H. gratefully acknowledges funding by the China Scholarship Council. N.I. was partly supported by the GOA program from KU Leuven and the scientific research grant R-143-000-A80-114 of the National University of Singapore. The computational resources and services used in this work were provided by the VSC (Flemish Supercomputer Center) funded by the Research Foundation - Flanders (FWO) and the Flemish Government - department EWI. This work was funded by the Researchers Supporting Project Number (RSP-2020/267) King Saud University, Riyadh, Saudi Arabia.

TABLE IX. The contribution from acoustic modes to warping parameter, Δ_{ac} , and its components (in meV).

	fcc						A15	
	K ₃ C ₆₀		Rb ₃ C ₆₀		Cs ₃ C ₆₀		Cs ₃ C ₆₀	
	LDA	PBE	LDA	PBE	LDA	PBE	LDA	PBE
F ^a	-0.048	-0.232	0.107	-0.263	0.256	0.093	-0.031	-0.021
	0.392	-0.112	0.815	-0.130	1.379	0.174	0.008	0.049
A ^a	3.747	0.407	4.824	-0.003	5.191	0.480	0.035	0.119
	3.617	0.395	4.747	-0.024	5.149	0.458	0.132	0.212
FF ^a	-0.002	-0.015	0.005	-0.010	0.006	-0.004	0.014	0.005
	-0.001	-0.006	0.002	-0.005	0.003	0.001	0.019	0.010
A-F	0.060	0.034	0.125	0.016	0.178	0.014	-0.037	0.012
F-FF	-0.028	-0.059	-0.021	-0.035	-0.032	-0.051	-0.003	0.001
A-FF	0.013	0.020	0.011	0.008	0.010	0.010	-0.017	-0.016
Δ_{ac}	3.741	0.155	5.051	-0.286	5.610	0.542	-0.040	0.100

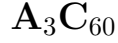
^aThe data in the second row correspond to the neglect of off-diagonal contributions after μ .

- [1] O. Gunnarsson, “Superconductivity in fullerides,” *Reviews of Modern Physics* **69**, 575–606 (1997).
- [2] K. Tanigaki, I. Hirotsawa, T. W. Ebbesen, J. Mizuki, Shimakawa, Y. Kubo, J. S. Tsai, and S. Kuroshima, “Superconductivity in sodium-and lithium-containing alkali-metal fullerides,” *Nature* **356**, 419–421 (1992).
- [3] A. Y. Ganin, Y. Takabayashi, Y. Z. Khimiyak, S. Margadonna, A. Tamai, M. J. Rosseinsky, and K. Prassides, “Bulk superconductivity at 38 K in a molecular system,” *Nat Mater* **7**, 367–71 (2008).
- [4] Y. Takabayashi, A. Y. Ganin, P. Jeglič, D. Arčon, T. Takano, Y. Iwasa, Y. Ohishi, M. Takata, N. Takeshita, K. Prassides, and M. J. Rosseinsky, “The Disorder-Free Non-BCS Superconductor Cs₃C₆₀ Emerges from an Antiferromagnetic Insulator Parent State,” *Science* **323**, 1585–1590 (2009).
- [5] Alexey Y. Ganin, Yasuhiro Takabayashi, Peter Jegli, Denis Aron, Anton Potonik, Peter J. Baker, Yasuo Ohishi, Martin T. McDonald, Manolis D. Tzirakis, Alec McLennan, George R. Darling, Masaki Takata, Matthew J. Rosseinsky, and Kosmas Prassides, “Polymorphism control of superconductivity and magnetism in Cs₃C₆₀ close to the Mott transition,” *Nature* **466**, 221–225 (2010).
- [6] M. Mitran, A. Cantaluppi, D. Nicoletti, S. Kaiser, A. Perucchi, S. Lupi, P. Di Pietro, D. Pontiroli, M. Riccò, S. R. Clark, D. Jaksch, and A. Cavalleri, “Possible light-induced superconductivity in K₃C₆₀ at high temperature,” *Nature* **530**, 461 (2016).
- [7] A. Cantaluppi, M. Buzzi, G. Jotzu, D. Nicoletti, M. Mitran, D. Pontiroli, M. Riccò, A. Perucchi, P. Di Pietro, and A. Cavalleri, “Pressure tuning of light-induced superconductivity in K₃C₆₀,” *Nat. Phys.* **14**, 837 (2018).
- [8] T. Yildirim, L. Barbedette, J. E. Fischer, C. L. Lin, J. Robert, P. Petit, and T. T. M. Palstra, “ T_c vs carrier concentration in cubic fulleride superconductors,” *Physical Review Letters* **77**, 167–170 (1996).
- [9] R. Kerkoud, P. Auban-Senzier, D. Jerome, S. Brazovskii, I. Luk’Yanchuk, N. Kirova, F. Rachdi, and C. Goze, “Insulator-metal transition in Rb₄C₆₀ under pressure from ¹³C-NMR,” *Journal of Physics and Chemistry of Solids* **57**, 143–152 (1996).
- [10] Y. Ihara, H. Alloul, P. Wzietek, D. Pontiroli, M. Mazzani, and M. Riccò, “NMR Study of the Mott Transitions to Superconductivity in the Two Cs₃C₆₀ Phases,” *Phys. Rev. Lett.* **104**, 256402 (2010).
- [11] A. Nava, C. Giannetti, A. Georges, E. Tosatti, and M. Fabrizio, “Cooling quasiparticles in A₃C₆₀ fullerides by excitonic mid-infrared absorption,” *Nature Physics* **14**, 154–159 (2018).
- [12] R. H. Zadik, Y. Takabayashi, G. Klupp, R. H. Colman, A. Y. Ganin, A. Potočník, P. Jeglič, D. Arčon, P. Matus, K. Kamarás, Y. Kasahara, Y. Iwasa, A. N. Fitch, Y. Ohishi, G. Garbarino, K. Kato, M. J. Rosseinsky, and K. Prassides, “Optimized unconventional superconductivity in a molecular Jahn-Teller metal,” *Sci. Adv.* **1**, e1500059 (2015).
- [13] N. Iwahara and L. F. Chibotaru, “Dynamical Jahn-Teller instability in metallic fullerides,” *Phys. Rev. B* **91**, 035109 (2015).
- [14] N. Iwahara, T. Sato, K. Tanaka, and L. F. Chibotaru, “Vibronic coupling in C₆₀⁻ anion revisited: Derivations from photoelectron spectra and DFT calculations,” *Phys. Rev. B* **82**, 245409 (2010).
- [15] Z. Huang and D. Liu, “Dynamical Jahn-Teller effect in the first excited C₆₀⁻,” *International Journal of Quantum Chemistry* **120**, e26148 (2020), <https://onlinelibrary.wiley.com/doi/pdf/10.1002/qua.26148>.
- [16] S. L. Altmann and P. Herzog, *Point-Group Theory Tables* (Clarendon Press, Oxford, 1994).
- [17] G. Klupp, P. Matus, K. Kamarás, A. Y. Ganin, A. McLennan, M. J. Rosseinsky, Y. Takabayashi, M. T. McDonald, and K. Prassides, “Dynamic Jahn-Teller effect in the parent insulating state of the molecular superconductor Cs₃C₆₀,” *Nat. Commun.* **3**, 912 (2012).
- [18] K. Kamarás, G. Klupp, P. Matus, A. Y. Ganin, A. McLennan, M. J. Rosseinsky, Y. Takabayashi, M. T.

- McDonald, and K. Prassides, “Mott localization in the correlated superconductor Cs_3C_{60} resulting from the molecular Jahn-Teller effect,” *J. Phys.: Conf. Ser.* **428**, 012002 (2013).
- [19] A. Potočnik, A. Y. Ganin, Y. Takabayashi, M. T. McDonald, I. Heinmaa, P. Jeglič, R. Stern, M. J. Rosseinsky, K. Prassides, and D. Arčon, “Jahn-Teller orbital glass state in the expanded fcc Cs_3C_{60} fulleride,” *Chem. Sci.* **5**, 3008 (2014).
- [20] I. Bersuker, *The Jahn-Teller Effect* (Cambridge University Press, 2006).
- [21] M. C. M. O’Brien, “Dynamic Jahn-Teller Effect in an Orbital Triplet State Coupled to Both E_g and T_{2g} Vibrations,” *Phys. Rev.* **187**, 407 (1969).
- [22] C. C. Chancey and M. C. M. O’Brien, *The Jahn-Teller Effect in C_{60} and Other Icosahedral Complexes* (Princeton University Press, Princeton, 1997).
- [23] P. Durand, G. R. Darling, Y. Dubitsky, A. Zaopo, and M. J. Rosseinsky, “The Mott-Hubbard insulating state and orbital degeneracy in the superconducting C_{60}^{3-} fulleride family,” *Nature materials* **2**, 605–610 (2003).
- [24] L. F. Chibotaru, “Spin-Vibronic Superexchange in Mott-Hubbard Fullerenes,” *Phys. Rev. Lett.* **94**, 186405 (2005).
- [25] V. Brouet, H. Alloul, S. Garaj, and L. Forró, “Persistence of molecular excitations in metallic fullerenes and their role in a possible metal to insulator transition at high temperatures,” *Phys. Rev. B* **66**, 155124 (2002).
- [26] P. W. Stephens, L. Mihaly, P. L. Lee, R. L. Whetten, S. M. Huang, R. Kaner, F. Deiderich, and K. Holczer, “Structure of single-phase superconducting K_3C_{60} ,” *Nature* **351**, 632–634 (1991).
- [27] S. Teslic, T. Egami, and J. E. Fischer, “Short-range antiferromagnetic orientational correlations in Rb_3C_{60} ,” *Physical Review B* **51**, 5973–5976 (1995).
- [28] H. Mazin, I. I., A. I. Liechtenstein, O. Gunnarsson, O. K. Andersen, V. P. Antropov, and S. E. Burkov, “Orientational order in A_3C_{60} : Antiferromagnetic Ising model for the fcc lattice,” *Phys Rev Lett* **70**, 4142–4145 (1993).
- [29] Tohru Sato, Ken Tokunaga, and Kazuyoshi Tanaka, “Vibronic coupling in cyclopentadienyl radical: A method for calculation of vibronic coupling constant and vibronic coupling density analysis,” *The Journal of Chemical Physics* **124**, 024314 (2006).
- [30] M. J. Frisch, G. W. Trucks, H. B. Schlegel, G. E. Scuseria, M. A. Robb, J. R. Cheeseman, G. Scalmani, V. Barone, G. A. Petersson, H. Nakatsuji, X. Li, M. Caricato, A. Marenich, J. Bloino, B. G. Janesko, R. Gomperts, B. Mennucci, H. P. Hratchian, J. V. Ortiz, A. F. Izmaylov, J. L. Sonnenberg, D. Williams-Young, F. Ding, F. Lipparini, F. Egidi, J. Goings, B. Peng, A. Petrone, T. Henderson, D. Ranasinghe, V. G. Zakrzewski, J. Gao, N. Rega, G. Zheng, W. Liang, M. Hada, M. Ehara, K. Toyota, R. Fukuda, J. Hasegawa, M. Ishida, T. Nakaajima, Y. Honda, O. Kitao, H. Nakai, T. Vreven, K. Throssell, J. A. Montgomery, J. E. Peralta Jr., F. Ogliaro, M. Bearpark, J. J. Heyd, E. Brothers, K. N. Kudin, V. N. Staroverov, T. Keith, R. Kobayashi, J. Normand, K. Raghavachari, A. Rendell, J. C. Burant, S. S. Iyengar, J. Tomasi, M. Cossi, J. M. Millam, M. Klene, C. Adamo, R. Cammi, J. W. Ochterski, R. L. Martin, K. Morokuma, O. Farkas, J. B. Foresman, and D. J. Fox, *Gaussian 09, Revision B.01*, Wallingford, CT (2009).
- [31] Axel D. Becke, “Density-functional thermochemistry. III. The role of exact exchange,” *The Journal of Chemical Physics* **98**, 5648–5652 (1993), <https://doi.org/10.1063/1.464913>.
- [32] D. Liu, Y. Niwa, N. Iwahara, T. Sato, and L. F. Chibotaru, “Quadratic Jahn-Teller effect of fullerene anions,” *Phys. Rev. B* **98**, 035402 (2018).
- [33] The Supplementary Material contains active intr Fullerene normal vibrational modes, alkali and inter-fullerene active displacements; details of pseudopotential generation for phonon calculations, full phonon dispersion; calculation of the effect of multiplet splitting on the adiabatic potential on one fullerene site; analysis of elastic response function to JT displacements at one site.
- [34] J. Q. You, J. R. Yan, and X. H. Yan, “Lattice dynamics of A_3C_{60} fullerenes, where the A are alkali-metal elements,” *Journal of Physics: Condensed Matter* **5**, L591 (1993).
- [35] R. Akashi and R. Arita, “Nonempirical study of superconductivity in alkali-doped fullerenes based on density functional theory for superconductors,” *Physical Review B* **88**, 054510 (2013).
- [36] Y. Nomura and R. Arita, “Ab initio downfolding for electron-phonon-coupled systems: Constrained density-functional perturbation theory,” *Physical Review B* **92** (2015), 10.1103/PhysRevB.92.245108.
- [37] S. Baroni, S. de Gironcoli, A. Dal Corso, and P. Giannozzi, “Phonons and related crystal properties from density-functional perturbation theory,” *Rev. Mod. Phys.* **73**, 515–562 (2001).
- [38] J. P. Perdew and Alex Zunger, “Self-interaction correction to density-functional approximations for many-electron systems,” *Phys. Rev. B* **23**, 5048–5079 (1981).
- [39] J. P. Perdew, K. Burke, and M. Ernzerhof, “Generalized Gradient Approximation Made Simple,” *Physical Review Letters* **77**, 3865–3868 (1996).
- [40] S. G. Louie, S. Froyen, and M. L. Cohen, “Nonlinear ionic pseudopotentials in spin-density-functional calculations,” *Physical Review B* **26**, 1738–1742 (1982).
- [41] D. D. Koelling and B. N. Harmon, “A technique for relativistic spin-polarised calculations,” *Journal of Physics C: Solid State Physics* **10**, 3107 (1977).
- [42] N. Troullier and Jos Luriaas Martins, “Efficient pseudopotentials for plane-wave calculations,” *Physical Review B* **43**, 1993–2006 (1991).
- [43] P. Giannozzi, S. Baroni, N. Bonini, M. Calandra, R. Car, C. Cavazzoni, D. Ceresoli, G. L. Chiarotti, M. Cococcioni, I. Dabo, A. Dal Corso, S. de Gironcoli, S. Fabris, G. Fratesi, R. Gebauer, U. Gerstmann, C. Gougoussis, A. Kokalj, M. Lazzeri, L. Martin-Samos, N. Marzari, F. Mauri, R. Mazzarello, S. Paolini, A. Pasquarello, L. Paulatto, C. Sbraccia, S. Scandolo, G. Sclauzero, A. P. Seitsonen, A. Smogunov, P. Umari, and R. M. Wentzcovitch, “QUANTUM ESPRESSO: a modular and open-source software project for quantum simulations of materials,” *Journal of Physics: Condensed Matter* **21**, 395502 (2009).
- [44] P. Zhou, K. Wang, A. M. Rao, P. C. Eklund, G. Dresselhaus, and M. S. Dresselhaus, “Raman-scattering studies of homogeneous K_3C_{60} films,” *Physical Review B* **45**, 10838–10840 (1992).
- [45] P. Zhou, K. Wang, P. C. Eklund, G. Dresselhaus, and M. S. Dresselhaus, “Raman-scattering study of the electron-phonon interaction in M_3C_{60} ($\text{M}=\text{K},\text{Rb}$),” *Physical Review B* **48**, 8412–8417 (1993).

- [46] M.G. Mitch, S.J. Chase, and J.S. Lannin, “Raman scattering and superconductivity of A_xC_{60} ,” *International Journal of Modern Physics B* **06**, 4013–4018 (1992).
- [47] M. G. Mitch and J. S. Lannin, “Raman scattering and electron-phonon coupling in A_3C_{60} ,” *Journal of Physics and Chemistry of Solids* **54**, 1801–1816 (1993).
- [48] U. Öpik and Maurice Henry Lecomte Pryce, “Studies of the Jahn-Teller effect. I. A survey of the static problem,” *Proceedings of the Royal Society of London. Series A. Mathematical and Physical Sciences* **238**, 425–447 (1957).
- [49] A. Ceulemans and L. F. Chibotaru, “Isostationary functions for multimode and multilevel Jahn-Teller systems,” *Theoretica chimica acta* **94**, 205–212 (1996).
- [50] A. Auerbach, N. Manini, and E. Tosatti, “Electron-vibron interactions in charged fullerenes. I. Berry phases,” *Phys. Rev. B* **49**, 12998 (1994).
- [51] M. C. M. O’Brien, “Vibronic energies in C_{60}^{n-} and the Jahn-Teller effect,” *Phys. Rev. B* **53**, 3775 (1996).
- [52] J. H. Van Vleck, “Paramagnetic relaxation times for titanium and chrome alum,” *Phys. Rev.* **57**, 426–447 (1940).
- [53] L. Chibotaru, “Effective Hamiltonian for multimode static Jahn-Teller effect in polycentre vibronic systems,” *Journal of Physics A: Mathematical and General* **27**, 6919 (1994).
- [54] N. Iwahara and L. F. Chibotaru, “Dynamical Jahn-Teller Effect and Antiferromagnetism in Cs_3C_{60} ,” *Phys. Rev. Lett.* **111**, 056401 (2013).
- [55] D. Liu, N. Iwahara, and L. F. Chibotaru, “Dynamical Jahn-Teller effect of fullerene anions,” *Physical Review B* **97** (2018), 10.1103/PhysRevB.97.115412.
- [56] L.F. Chibotaru, “Microscopic Approach to Cooperative Jahn-Teller Effect in Crystals with Strong Intra-Site Vibronic Coupling,” in *Advances in Quantum Chemistry*, Vol. 44 (Academic Press, 2003) pp. 649 – 667.
- [57] A. Abragam and B. Bleaney, *Electron Paramagnetic Resonance of Transition Ions* (Oxford : Clarendon press, 1970).
- [58] M.D Kaplan and V. G. Vehter, *Cooperative Phenomena in Jahn-Teller Crystals* (Springer US, New York, 1995).
- [59] Naoya Iwahara and Liviu F. Chibotaru, “Orbital disproportionation of electronic density is a universal feature of alkali-doped fullerenes,” *Nature Communications* **7**, 13093 (2016).
- [60] Naoya Iwahara, Tohru Sato, Kazuyoshi Tanaka, and Liviu F. Chibotaru, “Mechanisms of localization in isotope-substituted dynamical Jahn-Teller systems,” *EPL (Europhysics Letters)* **100**, 43001 (2012).
- [61] Yuki Matsuda, Naoya Iwahara, Katsumi Tanigaki, and Liviu F. Chibotaru, “Manifestation of vibronic dynamics in infrared spectra of mott insulating fullerenes,” *Phys. Rev. B* **98**, 165410 (2018).

Supplementary Material: Jahn-Teller effect in cubic fullerenes



Zhishuo Huang,¹ Munirah D. Albaqami,² Tohru Sato,³

Naoya Iwahara,^{4,1,5,*} and Liviu F. Chibotaru^{1,†}

¹*Theory of Nanomaterials Group, KU Leuven,
Celestijnenlaan 200F, B-3001 Leuven, Belgium*

²*Chemistry Department, College of Science, King Saud University,
P.O. Box 2455, Riyadh 11451, Saudi Arabia*

³*Fukui Institute for Fundamental Chemistry, Kyoto University,
Takano Nishihiraki-cho 34-4, Sakyo-ku, Kyoto 6068103, Japan*

⁴*Department of Chemistry, National University of Singapore,
Block S8 Level 3, 3 Science Drive 3, 117543, Singapore*

⁵*Graduate School of Engineering, Chiba University,
1-33 Yayoi-cho, Inage-ku, Chiba 263-8522, Japan*

(Dated: March 26, 2021)

I. CRYSTAL CONSTANTS

TABLE I. Lattice constants a of A_3C_{60} used in phonon calculations.

	$K_3C_{60}^1$	$Rb_3C_{60}^1$	$Cs_3C_{60}^2$	A15 $Cs_3C_{60}^2$
$a(\text{\AA})$	14.240	14.384	14.793	11.784

II. GENERATION AND TEST OF IONIZED PSEUDOPOTENTIAL

Energies of different elements for final consistency check were shown in Table II, from which we could see that the energy differences of all the generated PP gave the same energy level corresponding to AE calculation, except for Rb, of which the energy difference was less than 0.1 mRy, nearly to zero. As a further check, the pseudized Kohn-Sham orbitals and the logarithmic derivatives were compared, as plotted in Fig.1 and Fig.2. For both PBE and PZ PPs, the pseudized wavefunctions ($\Psi_{nl}(\mathbf{r})$, right column) went directly and smoothly to zero, with no wiggles or other strange features. For logarithmic derivatives (Dlog, left column), the AE orbitals and PP orbitals matched very well, and slightly deviations appeared only at relatively high ($> 1\text{Ry}$) energies.

In order to confirm good the ionized PPs were good enough for use, it should be tested whether these generated PPs could give or not the nearly same information when applied in real calculations of A_3C_{60} . All the calculations were performed by package Quantum Espresso[3] with the most used calculation parameters[4,5]: 60 Ry for cutoff energy for the wave functions, $4\times 4\times 4$ for Monkhorst-Pack grids of K points with 0.010 Ry for the Gaussian smearing. As we could see, the band structure of ionized PPs had a very good consistence with that of general PPs provided by Quantum Espresso PP library, with a slight dismatched at Γ point which was only about 0.02 eV, which, to some extent, showed that the generation of ionized PPs was successful and the generated PPs behave very well in describing A_3C_{60} system.

III. FULL PHONON DISPERSION AND ELASTIC COUPLING CONSTANTS

The full phonon dispersion for A_3C_{60} is shown in Fig. 3. The acoustic and optical phonon modes were transformed into the localized modes with the similar method as the construction

of the Wannier orbitals from the band orbitals. All the elastic coupling constants were shown in the attached txt files. Here is a short description for these attachments. The files were named by the notation of “ECC” with respect to each system. Taking “ECC_K_PB000” for an example, this means the information contained in this file is the elastic coupling constants between the local vibrational modes in the origin unit cell (labelled by $\mathbf{R} = (0,0,0)$) and that in the next unit cell (labelled by $\mathbf{R} = (0,0,0)$), while “ECC_K_PB001” means the information contained in this file is the elastic coupling constants between the local vibrational modes in the origin unit cell (labelled by $\mathbf{R} = (0,0,0)$) and that in the next unit cell (labelled by $\mathbf{R} = (0,0,0)$). For the information listed in these files, the first 3 columns contain the information of local vibration modes. The first column labels the symmetry type of local vibration modes, 1 for A_g , 2 for A_u , 3 for G_g , 4 for G_u , 5 for H_g , 6 for H_u , 7 for T_{1g} , 8 for T_{1u} , 9 for T_{2g} , 10 for T_{2u} , 11 for translational modes, 12 for pure rotational modes of fullerene modes, and 13 for normal modes of alkali-atoms. For A15, there are two extra labels, which are 14 for pure rotational modes of the second fullerene molecule sitting on the center of the unit cell, and 15 for the vibronic modes between two types of fullerene. The second column showed the i th order of each type of local modes.

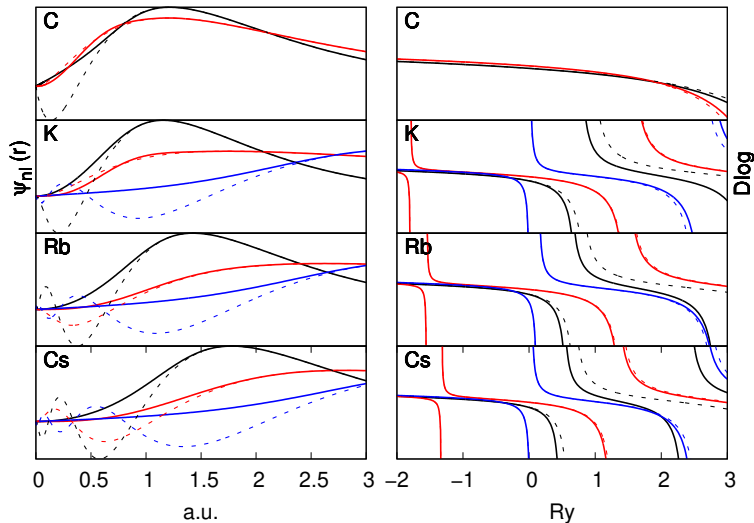


FIG. 1. GGA-PBE PPs, the comparison of the pseudized Kohn-Sham orbitals ($\Psi_{nl}(\mathbf{r})$, right column) and logarithmic derivatives (Dlog, left column) for C, K, Rb, and Cs. Solid line and dashed line represented the calculation from PPs and AE, correspondingly, and black, red, and blue accounted for s, p, and d orbital, respectively.

And the third column had the vibrational frequency, main fro the local modes obtained within fullerene molecule, of which we set all the frequencies for the vibrational modes of translational, pure rotational and alkli-atoms to 0. The unit for the frequencies are cm^{-1} , for the elastic coupling constants are Rydberg.

IV. JT ACTIVE VIBRATION MODES

A. JT active vibration modes of Fullerene

The symmetrization of the mass-weighted normal modes were done by using projection operator. The symmetrized normal modes were shown below (Figs. 4 and 5).

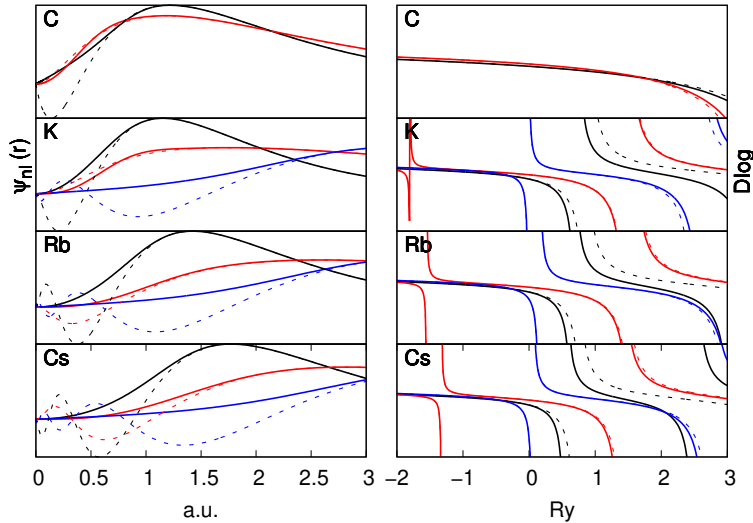


FIG. 2. LDA-PZ PPs, the comparison of the pseudized Kohn-Sham orbitals ($\Psi_{nl}(\mathbf{r})$, right column) and logarithmic derivatives (Dlog, left column) for C, K, Rb, and Cs. Solid line and dashed line represented the calculation from PPs and AE, correspondingly, and black, red, and blue accounted for s, p, and d orbital, respectively.

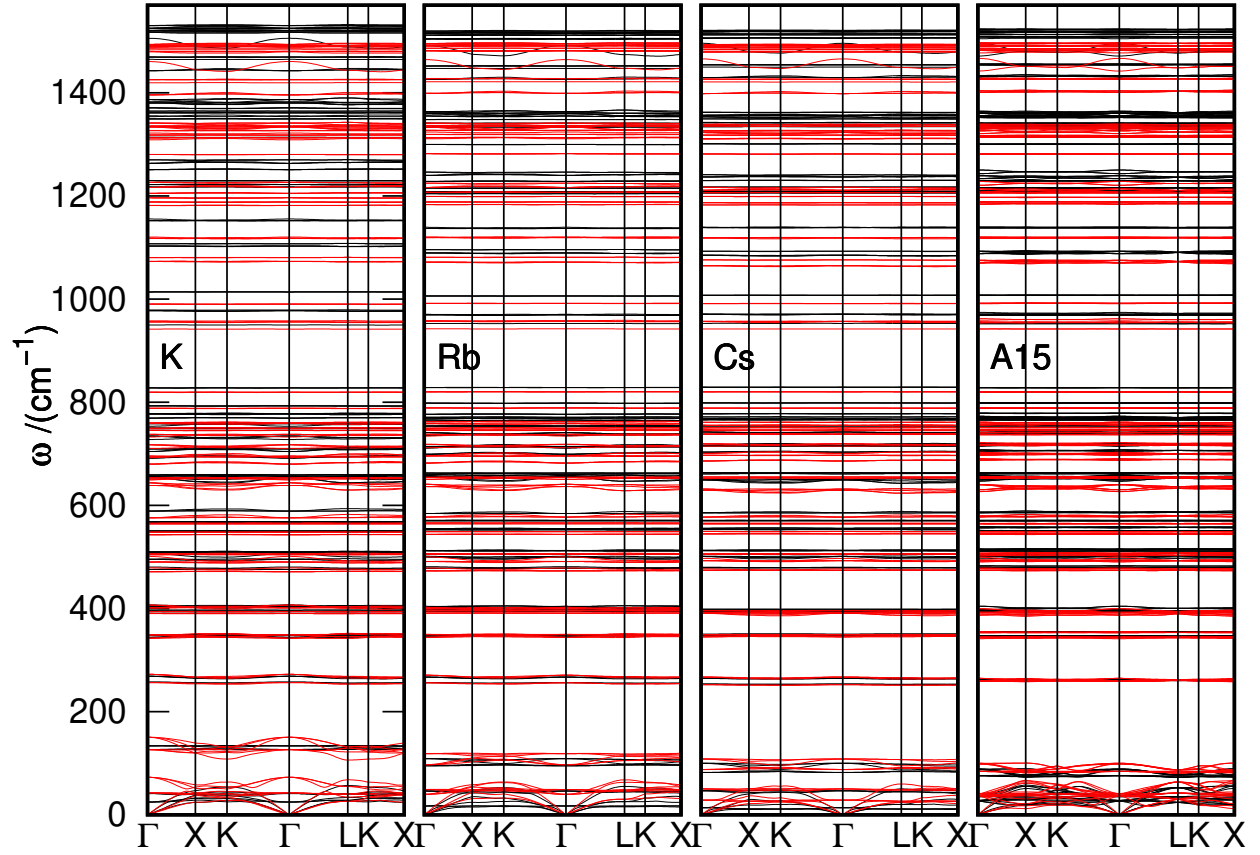


FIG. 3. GGA-PBE PPs, the comparison of the pseudized Kohn-Sham orbitals ($\Psi_{nl}(\mathbf{r})$, right column) and logarithmic derivatives (Dlog, left column) for C, K, Rb, and Cs. Solid line and dashed line represented the calculation from PPs and AE, correspondingly, and black, red, and blue accounted for s, p, and d orbital, respectively.

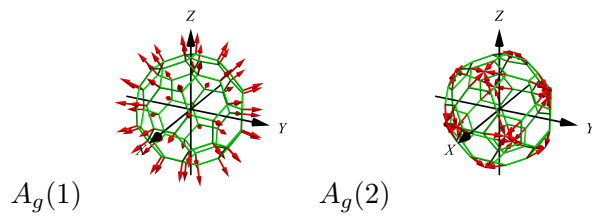


FIG. 4. Schematic representation of A_g modes

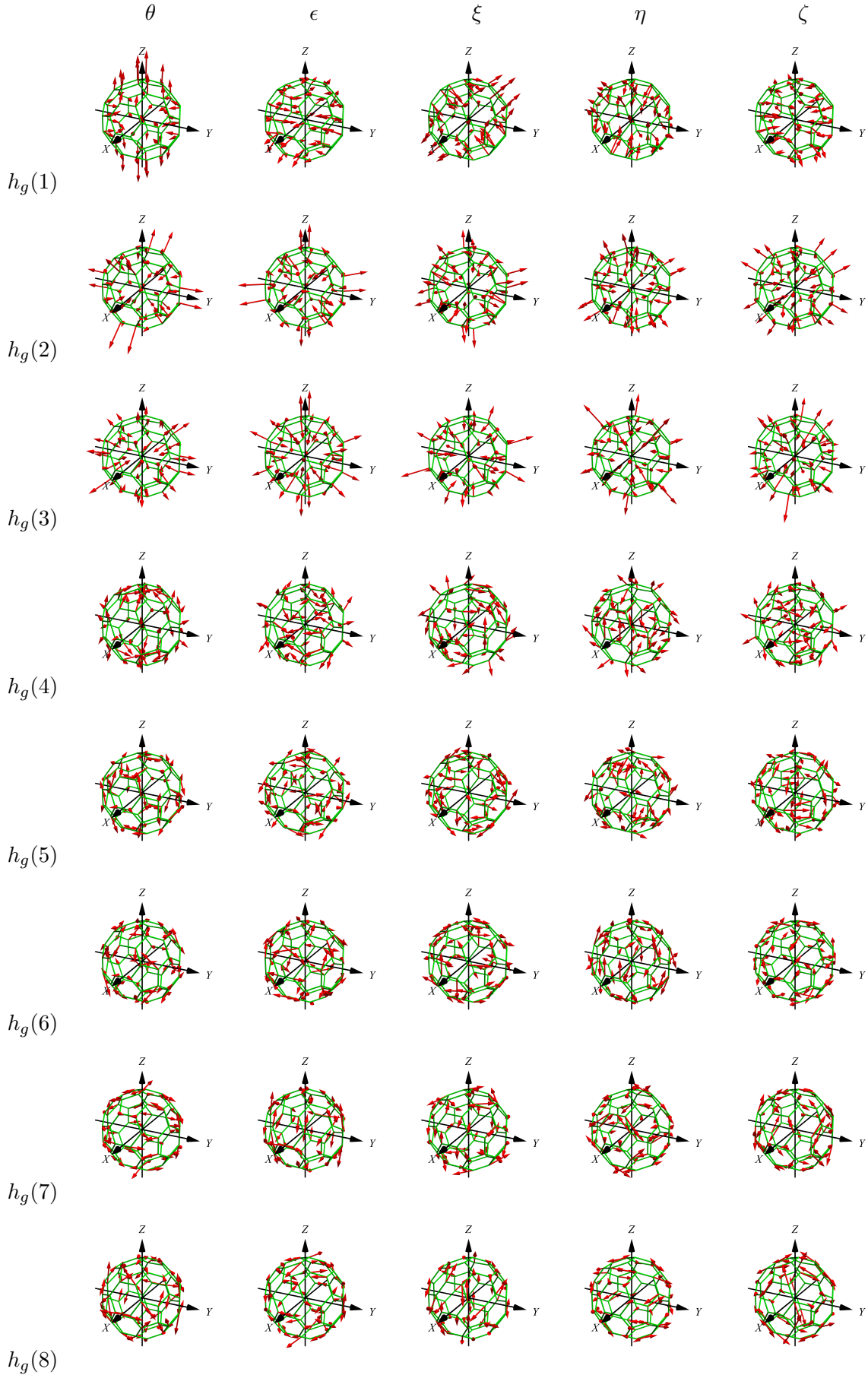


FIG. 5. Schematic representation of H_q modes

B. Symmetry adapted alkali JT active modes

Structures and coordinates of octahedron and cube are shown in Fig. 6 ((a) and (b)) and Table IV.

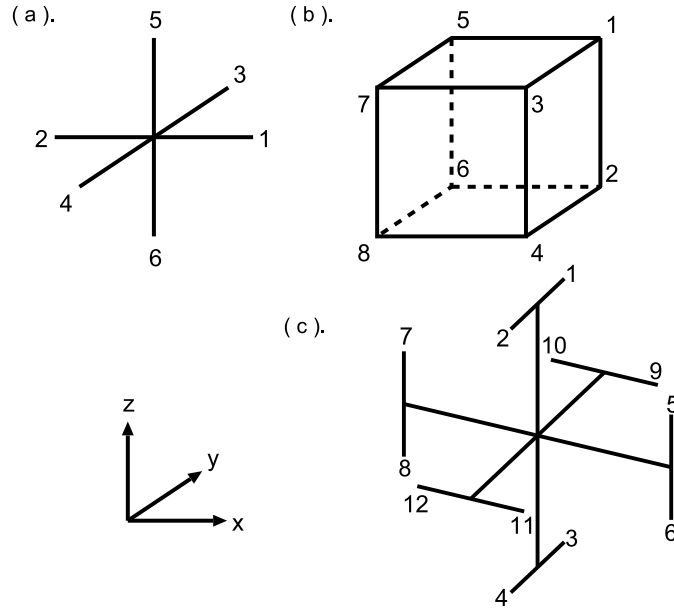


FIG. 6. Structures of alkali atom in both FCC and BCC structures. (a) and (b) correspond to octahedron and cube, respectively, and (c) represents pseudo-octahedron.

TABLE IV. Coordinates of octahedron, cube and pseudo-octahedron Akali atoms.

	octahedron	cube	pseudo-octahedron
A1	(1, 0, 0)	1/2(1, 1, 1)	1/4(2, 1, 0)
A2	(-1, 0, 0)	1/2(1, 1, -1)	1/4(2, 1, 0)
A3	(0, 1, 0)	1/2(1, -1, 1)	1/4(-2, -1, 0)
A4	(0, -1, 0)	1/2(1, -1, -1)	1/4(-2, 1, 0)
A5	(0, 0, 1)	1/2(-1, 1, 1)	1/4(0, -2, 1)
A6	(0, 0, -1)	1/2(-1, 1, -1)	1/4(0, 2, -1)
A7	-	1/2(-1, -1, 1)	1/4(0, 2, 1)
A8	-	1/2(-1, -1, -1)	1/4(0, -2, -1)
A9	-	1/2(-1, -1, -1)	1/4(-1, 0, -2)
A10	-	1/2(-1, -1, -1)	1/4(1, 0, -2)
A11	-	1/2(-1, -1, -1)	1/4(-1, 0, 2)
A12	-	1/2(-1, -1, -1)	1/4(1, 0, 2)

The irreducible representation of LUMO is t_{1u} . The orbital couples to A_{1g} , E_g , and T_{2g} vibrational modes. And the symmetry adapted vibrational vectors for cube, octahedron, and pseudo-octahedron are given in Tables V, VI, and VII, respectively.

TABLE V. Symmetry adapted modes of octahedron

	a_{1g}	e_g	t_{2g}	
		θ	ζ	
			ϵ	
A1	$\frac{1}{\sqrt{6}}(1, 0, 0)$	$\frac{1}{2\sqrt{3}}(-1, 0, 0)$	$\frac{1}{2}(1, 0, 0)$	$\frac{1}{2}(0, 1, 0)$
A2	$\frac{1}{\sqrt{6}}(-1, 0, 0)$	$\frac{1}{2\sqrt{3}}(1, 0, 0)$	$\frac{1}{2}(-1, 0, 0)$	$\frac{1}{2}(0, -1, 0)$
A3	$\frac{1}{\sqrt{6}}(0, 1, 0)$	$\frac{1}{2\sqrt{3}}(0, -1, 0)$	$\frac{1}{2}(0, -1, 0)$	$\frac{1}{2}(1, 0, 0)$
A4	$\frac{1}{\sqrt{6}}(0, -1, 0)$	$\frac{1}{2\sqrt{3}}(0, 1, 0)$	$\frac{1}{2}(0, 1, 0)$	$\frac{1}{2}(-1, 0, 0)$
A5	$\frac{1}{\sqrt{6}}(0, 0, 1)$	$\frac{1}{2\sqrt{3}}(0, 0, 2)$	(0, 0, 0)	(0, 0, 0)
A6	$\frac{1}{\sqrt{6}}(0, 0, -1)$	$\frac{1}{2\sqrt{3}}(0, 0, -2)$	(0, 0, 0)	(0, 0, 0)

TABLE VI. Symmetry adapted modes of cube

	a_{1g}	e_g		$t_{2g}(1)$	$t_{2g}(2)$
		θ	ϵ		
A1	$\frac{1}{\sqrt{24}}(1, 1, 1)$	$\frac{1}{\sqrt{48}}(-1, -1, 2)$	$\frac{1}{4}(1, -1, 0)$	$\frac{1}{\sqrt{24}}(1, 1, 1)$	$\frac{1}{\sqrt{48}}(1, 1, -2)$
A2	$\frac{1}{\sqrt{24}}(1, 1, -1)$	$\frac{1}{\sqrt{48}}(-1, -1, -2)$	$\frac{1}{4}(1, -1, 0)$	$\frac{1}{\sqrt{24}}(1, 1, -1)$	$\frac{1}{\sqrt{48}}(1, 1, 2)$
A3	$\frac{1}{\sqrt{24}}(1, -1, 1)$	$\frac{1}{\sqrt{48}}(-1, 1, 2)$	$\frac{1}{4}(1, 1, 0)$	$\frac{1}{\sqrt{24}}(-1, 1, -1)$	$\frac{1}{\sqrt{48}}(-1, 1, 2)$
A4	$\frac{1}{\sqrt{24}}(1, -1, -1)$	$\frac{1}{\sqrt{48}}(-1, 1, -2)$	$\frac{1}{4}(1, 1, 0)$	$\frac{1}{\sqrt{24}}(-1, 1, 1)$	$\frac{1}{\sqrt{48}}(-1, 1, -2)$
A5	$\frac{1}{\sqrt{24}}(-1, 1, 1)$	$\frac{1}{\sqrt{48}}(1, -1, 2)$	$\frac{1}{4}(-1, -1, 0)$	$\frac{1}{\sqrt{24}}(1, -1, -1)$	$\frac{1}{\sqrt{48}}(1, -1, 2)$
A6	$\frac{1}{\sqrt{24}}(-1, 1, -1)$	$\frac{1}{\sqrt{48}}(1, -1, -2)$	$\frac{1}{4}(-1, -1, 0)$	$\frac{1}{\sqrt{24}}(1, -1, 1)$	$\frac{1}{\sqrt{48}}(1, -1, -2)$
A7	$\frac{1}{\sqrt{24}}(-1, -1, 1)$	$\frac{1}{\sqrt{48}}(1, 1, 2)$	$\frac{1}{4}(-1, 1, 0)$	$\frac{1}{\sqrt{24}}(-1, -1, 1)$	$\frac{1}{\sqrt{48}}(-1, -1, -2)$
A8	$\frac{1}{\sqrt{24}}(-1, -1, -1)$	$\frac{1}{\sqrt{48}}(1, 1, -2)$	$\frac{1}{4}(-1, 1, 0)$	$\frac{1}{\sqrt{24}}(-1, -1, -1)$	$\frac{1}{\sqrt{48}}(-1, -1, 2)$

TABLE VII. Symmetry adapted modes of pseudo-octahedron

	$A_g(1)$			$E_{g\theta}(1)$			$E_{g\epsilon}(1)$		
A1	0.000000	0.247154	-0.149159	0.000000	0.149157	0.247155	-0.000000	0.009650	0.193490
A2	0.000000	-0.247154	-0.149159	0.000000	-0.149157	0.247155	-0.000000	-0.009650	0.193490
A3	0.000000	0.247154	0.149159	0.000000	0.149157	-0.247155	-0.000000	0.009660	-0.193490
A4	0.000000	-0.247154	0.149159	0.000000	-0.149157	-0.247155	-0.000000	-0.009650	-0.193490
A5	-0.149159	0.000000	0.247154	0.247155	0.000000	0.149157	0.202060	-0.000000	0.082150
A6	-0.149159	0.000000	-0.247154	0.247155	0.000000	-0.149157	0.202060	-0.000000	-0.082150
A7	0.149159	0.000000	0.247154	-0.247155	0.000000	0.149157	-0.202060	-0.000000	0.082150
A8	0.149159	0.000000	-0.247154	-0.247155	0.000000	-0.149157	-0.202060	-0.000000	-0.082150
A9	0.247154	-0.149159	0.000000	0.149157	0.247155	0.000000	-0.091800	-0.395550	-0.000000
A10	-0.247154	-0.149159	0.000000	-0.149157	0.247155	0.000000	0.091800	-0.395550	-0.000000
A11	0.247154	0.149159	0.000000	0.149157	-0.247155	0.000000	-0.091800	0.395550	-0.000000
A12	-0.247154	0.149159	0.000000	-0.149157	-0.247155	0.000000	0.091800	0.395550	-0.000000
	$A_g(2)$			$E_{g\theta}(2)$			$E_{g\epsilon}(2)$		
A1	0.000000	-0.100430	-0.345030	-0.000000	0.126520	-0.068090	0.000000	0.374810	-0.074450
A2	0.000000	0.100430	-0.345030	-0.000000	-0.126520	-0.068090	0.000000	-0.374810	-0.074450
A3	0.000000	-0.100430	0.345030	-0.000000	0.126520	0.068090	0.000000	0.374810	0.074450
A4	0.000000	0.100430	0.345030	-0.000000	-0.126520	0.068090	0.000000	-0.374810	0.074450
A5	0.340090	0.000000	0.058580	-0.030430	-0.000000	0.261330	0.096200	0.000000	-0.296970
A6	0.340080	0.000000	-0.058580	-0.030430	-0.000000	-0.261330	0.096200	0.000000	0.296970
A7	-0.340080	0.000000	0.058580	0.030430	-0.000000	0.261330	-0.096200	0.000000	-0.296970
A8	-0.340080	0.000000	-0.058580	0.030430	-0.000000	-0.261330	-0.096200	0.000000	0.296970
A9	0.041860	0.004950	0.000000	-0.387850	0.098520	-0.000000	-0.077840	-0.021740	0.000000
A10	-0.041860	0.004950	0.000000	0.387850	0.098530	-0.000000	0.077830	-0.021740	0.000000
A11	0.041860	-0.004950	0.000000	-0.387850	-0.098520	-0.000000	-0.077830	0.021740	0.000000
A12	-0.041860	-0.004950	0.000000	0.387850	-0.098530	-0.000000	0.077830	0.021740	0.000000
	$T_{2g\xi}(1)$			$T_{2g\xi}(2)$			$T_{2g\xi}(3)$		
A1	0.000000	-0.183513	0.143035	0.034419	-0.000000	-0.000000	0.441224	0.000000	0.000000
A2	0.000000	-0.183513	-0.143035	0.034419	-0.000000	-0.000000	-0.441224	0.000000	0.000000
A3	0.000000	0.183513	0.143035	-0.034419	-0.000000	-0.000000	0.441224	0.000000	0.000000
A4	0.000000	0.183513	-0.143035	-0.034419	-0.000000	-0.000000	-0.441224	0.000000	0.000000
A5	0.000000	0.441225	0.000000	-0.143036	-0.000000	0.183517	0.000000	-0.034417	0.000000
A6	0.000000	-0.441225	0.000000	0.143036	-0.000000	0.183517	0.000000	-0.034417	0.000000
A7	0.000000	0.441225	0.000000	-0.143036	-0.000000	-0.183517	0.000000	0.034417	0.000000
A8	0.000000	-0.441225	0.000000	0.143036	-0.000000	-0.183517	0.000000	0.034417	0.000000
A9	0.000000	0.000000	-0.034417	-0.000000	-0.000000	-0.441223	-0.183514	0.143037	0.000000
A10	0.000000	0.000000	-0.034417	-0.000000	-0.000000	0.441223	-0.183514	-0.143037	0.000000
A11	0.000000	0.000000	0.034417	-0.000000	-0.000000	-0.441223	0.183514	0.143037	0.000000
A12	0.000000	0.000000	0.034417	-0.000000	-0.000000	0.441223	0.183514	-0.143037	0.000000

And the symmetry adapted vibrational vectors for inter-fullerene in FCC and A15 cases are given in Tables VIII, IX, respectively.

TABLE VIII. Symmetry adapted modes of inter-fullerene of FCC fullerenes.

	A_g			$E_{g\theta}(1)$			$E_{ge}(1)$		
A1	0.000000	0.204124	0.204124	-0.000000	-0.142461	-0.146206	0.000000	-0.251075	-0.248911
A2	0.000000	-0.204124	0.204124	-0.000000	0.142461	-0.146206	0.000000	0.251075	-0.248911
A3	0.000000	-0.204124	-0.204124	-0.000000	0.142461	0.146206	0.000000	0.251075	0.248911
A4	0.000000	0.204124	-0.204124	-0.000000	-0.142461	0.146206	0.000000	-0.251075	0.248911
A5	0.204124	0.000000	0.204124	-0.142461	-0.000000	-0.146206	0.251075	0.000000	0.248911
A6	-0.204124	0.000000	0.204124	0.142461	-0.000000	-0.146206	-0.251075	0.000000	0.248911
A7	-0.204124	0.000000	-0.204124	0.142461	-0.000000	0.146206	-0.251075	0.000000	-0.248911
A8	0.204124	0.000000	-0.204124	-0.142461	-0.000000	0.146206	0.251075	0.000000	-0.248911
A9	0.204124	0.204124	0.000000	0.288667	0.288667	-0.000000	0.002164	-0.002164	0.000000
A10	-0.204124	0.204124	0.000000	-0.288667	0.288667	-0.000000	-0.002164	-0.002164	0.000000
A11	-0.204124	-0.204124	0.000000	-0.288667	-0.288667	-0.000000	-0.002164	0.002164	0.000000
A12	0.204124	-0.204124	0.000000	0.288667	-0.288667	-0.000000	0.002164	0.002164	0.000000
	$E_{g\theta}(2)$			$E_{ge}(2)$			$T_{2g\xi}(1)$		
A1	-0.000000	-0.251074	0.248911	0.000000	-0.142457	0.146210	0.000000	0.348929	0.348929
A2	-0.000000	0.251074	0.248911	0.000000	0.142457	0.146210	0.000000	0.348929	-0.348929
A3	-0.000000	0.251074	-0.248911	0.000000	0.142457	-0.146210	0.000000	-0.348929	-0.348929
A4	-0.000000	-0.251074	-0.248911	0.000000	-0.142457	-0.146210	0.000000	-0.348929	0.348929
A5	-0.251074	-0.000000	0.248911	0.142457	0.000000	-0.146210	0.000000	0.056999	0.000000
A6	0.251074	-0.000000	0.248911	-0.142457	0.000000	-0.146210	0.000000	0.056999	0.000000
A7	0.251074	-0.000000	-0.248911	-0.142457	0.000000	0.146210	0.000000	-0.056999	0.000000
A8	-0.251074	-0.000000	-0.248911	0.142457	0.000000	0.146210	0.000000	-0.056999	0.000000
A9	0.002163	0.002163	-0.000000	0.288667	-0.288667	0.000000	0.000000	0.000000	0.056999
A10	-0.002163	0.002163	-0.000000	-0.288667	-0.288667	0.000000	0.000000	0.000000	0.056999
A11	-0.002163	-0.002163	-0.000000	-0.288667	0.288667	0.000000	0.000000	0.000000	-0.056999
A12	0.002163	-0.002163	-0.000000	0.288667	0.288667	0.000000	0.000000	0.000000	-0.056999
	$T_{2g\xi}(2)$			-	-	-	-	-	-
A1	0.056997	0.000000	0.000000	-	-	-	-	-	-
A2	0.056997	0.000000	0.000000	-	-	-	-	-	-
A3	-0.056997	0.000000	0.000000	-	-	-	-	-	-
A4	-0.056997	0.000000	0.000000	-	-	-	-	-	-
A5	0.348929	0.000000	0.348929	-	-	-	-	-	-
A6	0.348929	0.000000	-0.348929	-	-	-	-	-	-
A7	-0.348929	0.000000	-0.348929	-	-	-	-	-	-
A8	-0.348929	0.000000	0.348929	-	-	-	-	-	-
A9	0.000000	0.000000	0.056997	-	-	-	-	-	-
A10	0.000000	0.000000	-0.056997	-	-	-	-	-	-
A11	0.000000	0.000000	-0.056997	-	-	-	-	-	-
A12	0.000000	0.000000	0.056997	-	-	-	-	-	-

TABLE IX. Symmetry adapted modes of inter-fullerene of A15.

	A_g			$E_{g\theta}$			$E_{g\epsilon}$		
A1	0.204124	0.204124	0.204124	-0.144338	-0.144338	0.288675	0.250000	-0.250000	0.000000
A2	-0.204124	0.204124	0.204124	0.144338	-0.144338	0.288675	-0.250000	-0.250000	0.000000
A3	0.204124	0.204124	-0.204124	-0.144338	-0.144338	-0.288675	0.250000	-0.250000	0.000000
A4	-0.204124	0.204124	-0.204124	0.144338	-0.144338	-0.288675	-0.250000	-0.250000	0.000000
A5	0.204124	-0.204124	0.204124	-0.144338	0.144338	0.288675	0.250000	0.250000	0.000000
A6	-0.204124	-0.204124	0.204124	0.144338	0.144338	0.288675	-0.250000	0.250000	0.000000
A7	0.204124	-0.204124	-0.204124	-0.144338	0.144338	-0.288675	0.250000	0.250000	0.000000
A8	-0.204124	-0.204124	-0.204124	0.144338	0.144338	-0.288675	-0.250000	0.250000	0.000000
	$T_{2g\xi}(1)$			$T_{2g\xi}(2)$			-		
A1	0.204124	0.204124	0.204124	0.144338	0.144338	-0.288675	-	-	-
A2	0.204124	-0.204124	-0.204124	0.144338	-0.144338	0.288675	-	-	-
A3	0.204124	0.204124	-0.204124	0.144338	0.144338	0.288675	-	-	-
A4	0.204124	-0.204124	0.204124	0.144338	-0.144338	-0.288675	-	-	-
A5	-0.204124	0.204124	-0.204124	-0.144338	0.144338	0.288675	-	-	-
A6	-0.204124	-0.204124	0.204124	-0.144338	-0.144338	-0.288675	-	-	-
A7	-0.204124	0.204124	0.204124	-0.144338	0.144338	-0.288675	-	-	-
A8	-0.204124	-0.204124	-0.204124	-0.144338	-0.144338	0.288675	-	-	-

V. ELASTIC COUPLING INFORMATION

VI. ADIABATIC POTENTIAL OF ISOLATED TRIVALENT C_{60}

The adiabatic potential energy surface of isolated C_{60}^{3-} is calculated. The model Hamiltonian consists of harmonic potential, Hund coupling \hat{H}_H , and linear Jahn-Teller coupling $\hat{V}_h = \hat{V}_e + \hat{V}_t$. The explicit forms of the Hund and Jahn-Teller couplings are given in Eqs. ((3) and (4) in the main text, respectively. The vibronic coupling parameters for the e and t_2 modes are the same, $V_e = V_t = V$.

For the analysis of the adiabatic potential energy surface, it is convenient to use the

adiabatic orbitals which diagonalizes \hat{V}_h :

$$\hat{H}_{JT} = \sum_{\sigma} Vq \left(\hat{a}_{1\sigma}^{\dagger}, \hat{a}_{2\sigma}^{\dagger}, \hat{a}_{3\sigma}^{\dagger} \right) \begin{pmatrix} -\cos\left(\alpha - \frac{2\pi}{3}\right) & 0 & 0 \\ 0 & -\cos\left(\alpha + \frac{2\pi}{3}\right) & 0 \\ 0 & 0 & -\cos\alpha \end{pmatrix} \begin{pmatrix} \hat{a}_{1\sigma} \\ \hat{a}_{2\sigma} \\ \hat{a}_{3\sigma} \end{pmatrix}. \quad (1)$$

q is the length of the H_g normal coordinates. See for details, Refs. O'Brien 1971, Auerbach 1994, O'Brien 1996, Iwahara 2018.

When the adiabatic orbitals are populated by three electrons without Jahn-Teller deformations, the Hund coupling splits the electron configurations into 4S , 2D and 2P terms. The Jahn-Teller effect is relevant to the doublet terms: The 2P term is higher in energy by $2J_H$ than 2D term.

The electronic states for the 2D terms are expressed by

$$\begin{aligned} & \frac{1}{\sqrt{6}} \left(2\hat{a}_{1\downarrow}^{\dagger}\hat{a}_{2\uparrow}^{\dagger}\hat{a}_{3\uparrow}^{\dagger} - \hat{a}_{1\uparrow}^{\dagger}\hat{a}_{2\downarrow}^{\dagger}\hat{a}_{3\uparrow}^{\dagger} - \hat{a}_{1\uparrow}^{\dagger}\hat{a}_{2\uparrow}^{\dagger}\hat{a}_{3\downarrow}^{\dagger} \right), \quad \frac{1}{\sqrt{2}} \left(\hat{a}_{1\uparrow}^{\dagger}\hat{a}_{2\downarrow}^{\dagger}\hat{a}_{3\uparrow}^{\dagger} - \hat{a}_{1\uparrow}^{\dagger}\hat{a}_{2\uparrow}^{\dagger}\hat{a}_{3\downarrow}^{\dagger} \right), \\ & \frac{1}{\sqrt{2}} \left(\hat{a}_{1\uparrow}^{\dagger}\hat{a}_{2\uparrow}^{\dagger}\hat{a}_{1\downarrow}^{\dagger} - \hat{a}_{2\uparrow}^{\dagger}\hat{a}_{3\uparrow}^{\dagger}\hat{a}_{3\downarrow}^{\dagger} \right), \quad \frac{1}{\sqrt{2}} \left(\hat{a}_{2\uparrow}^{\dagger}\hat{a}_{3\uparrow}^{\dagger}\hat{a}_{2\downarrow}^{\dagger} - \hat{a}_{3\uparrow}^{\dagger}\hat{a}_{1\uparrow}^{\dagger}\hat{a}_{1\downarrow}^{\dagger} \right), \quad \frac{1}{\sqrt{2}} \left(\hat{a}_{3\uparrow}^{\dagger}\hat{a}_{1\uparrow}^{\dagger}\hat{a}_{3\downarrow}^{\dagger} - \hat{a}_{1\uparrow}^{\dagger}\hat{a}_{2\uparrow}^{\dagger}\hat{a}_{2\downarrow}^{\dagger} \right), \end{aligned} \quad (2)$$

and those for the 2P term are

$$\frac{1}{\sqrt{2}} \left(\hat{a}_{3\uparrow}^{\dagger}\hat{a}_{1\uparrow}^{\dagger}\hat{a}_{3\downarrow}^{\dagger} + \hat{a}_{1\uparrow}^{\dagger}\hat{a}_{2\uparrow}^{\dagger}\hat{a}_{2\downarrow}^{\dagger} \right), \quad \frac{1}{\sqrt{2}} \left(\hat{a}_{1\uparrow}^{\dagger}\hat{a}_{2\uparrow}^{\dagger}\hat{a}_{1\downarrow}^{\dagger} + \hat{a}_{2\uparrow}^{\dagger}\hat{a}_{3\uparrow}^{\dagger}\hat{a}_{3\downarrow}^{\dagger} \right), \quad \frac{1}{\sqrt{2}} \left(\hat{a}_{2\uparrow}^{\dagger}\hat{a}_{3\uparrow}^{\dagger}\hat{a}_{2\downarrow}^{\dagger} + \hat{a}_{3\uparrow}^{\dagger}\hat{a}_{1\uparrow}^{\dagger}\hat{a}_{1\downarrow}^{\dagger} \right). \quad (3)$$

With the use of the multiplet states as the basis, the Jahn-Teller coupling matrix is written as

$$\begin{aligned} (\mathbf{V}_h)_{PD} &= Vq \begin{pmatrix} 0 & 0 & 0 & -\sin\left(\alpha + \frac{\pi}{6}\right) - \cos\alpha \\ 0 & 0 & \sin\left(-\alpha + \frac{\pi}{6}\right) + \cos\alpha & 0 \\ 0 & 0 & 0 & \sqrt{3}\sin\alpha \\ 0 & 0 & \sqrt{3}\sin\alpha & 0 \end{pmatrix}, \\ (\mathbf{V}_h)_{DP} &= [(\mathbf{V}_h)_{PD}]^T. \end{aligned} \quad (4)$$

The diagonal 3×3 and 5×5 blocks for the P and D terms are zero.

The eigenvalues of $\mathbf{H}_H + \mathbf{V}_h$ for the spin doublet terms are given as

$$\begin{aligned} & 0, \quad 0, \quad J_H \mp \sqrt{J_H^2 + 3[Vq\sin\alpha]^2}, \\ & J_H \mp \sqrt{J_H^2 + 3[Vq\cos\left(\alpha + \frac{\pi}{6}\right)]^2}, \quad J_H \mp \sqrt{J_H^2 + 3[Vq\cos\left(\alpha - \frac{\pi}{6}\right)]^2}. \end{aligned} \quad (5)$$

The minima of the APES locate at (elastic energy $\omega^2 q^2/2$ is considered too)

$$(q, \alpha) = \left(\frac{\sqrt{3}V}{\omega^2} \sqrt{1 - \left(\frac{J_H}{3V^2/\omega^2} \right)^2}, \frac{\pi}{2} \right), \quad (6)$$

with the Jahn-Teller stabilization energy

$$E_{\text{JT}}^{(3)} = J_H - \frac{3V^2}{2\omega^2} - \frac{J_H^2}{6V^2/\omega^2}. \quad (7)$$

The 2D term energy is used as the origin of the energy.

* naoya.iwahara@gmail.com

† liviu.chibotaru@kuleuven.be

¹ K. Tanigaki, I. Hirose, T. W. Ebbesen, J. Mizuki, Shimakawa, Y. Kubo, J. S. Tsai, and S. Kuroshima, *Nature* **356**, 419 (1992).

² A. Y. Ganin, Y. Takabayashi, Y. Z. Khimyak, S. Margadonna, A. Tamai, M. J. Rosseinsky, and K. Prassides, *Nat Mater* **7**, 367 (2008).

³ P. Giannozzi, S. Baroni, N. Bonini, M. Calandra, R. Car, C. Cavazzoni, D. Ceresoli, G. L. Chiarotti, M. Cococcioni, I. Dabo, A. D. Corso, S. de Gironcoli, S. Fabris, G. Fratesi, R. Gebauer, U. Gerstmann, C. Gougoussis, A. Kokalj, M. Lazzeri, L. Martin-Samos, N. Marzari, F. Mauri, R. Mazzarello, S. Paolini, A. Pasquarello, L. Paulatto, C. Sbraccia, S. Scandolo, G. Sclauzero, A. P. Seitsonen, A. Smogunov, P. Umari, and R. M. Wentzcovitch, *Journal of Physics: Condensed Matter* **21**, 395502 (2009).

⁴ Y. Nomura and R. Arita, *Physical Review B* **92** (2015), 10.1103/PhysRevB.92.245108.

⁵ R. Akashi and R. Arita, *Physical Review B* **88**, 054510 (2013).

⁶ P. Zhou, K. Wang, A. M. Rao, P. C. Eklund, G. Dresselhaus, and M. S. Dresselhaus, *Physical Review B* **45**, 10838 (1992).

⁷ M. Mitch, S. Chase, and J. Lannin, *International Journal of Modern Physics B* **06**, 4013 (1992).

⁸ M. G. Mitch and J. S. Lannin, *Journal of Physics and Chemistry of Solids* **54**, 1801 (1993).

⁹ P. Zhou, K. Wang, P. C. Eklund, G. Dresselhaus, and M. S. Dresselhaus, *Physical Review B* **48**, 8412 (1993).

TABLE II. Comparison of the final energy of all electron calculation (AE) E_{AE} , pseudopotential calculation (PS) E_{PS} , and the absolute difference between them ΔE for difference exchange-correlation functional (PBE and PZ) and difference elements (C, K, Rb, and Cs). n, l were principal quantum number and angular quantum number for pseudopotential, respectively. nl was the configuration of all-electron. Occu was the occupation of electron in the state. All the unit for energy was Ry

	E_{xc}	n	l	nl	Occu	E_{AE}	E_{PS}	ΔE
C	PBE	1	0	2S	1(2.00)	-1.00980	-1.00980	0.00000
		2	1	2P	1(2.00)	-0.38872	-0.38872	0.00000
	PZ	1	0	2S	1(2.00)	-1.00195	-1.00195	0.00000
		2	1	2P	1(2.00)	-0.39860	-0.39860	0.00000
K		2	1	3P	1(6.00)	-1.82985	-1.82985	0.00000
	PBE	3	2	3D	1(0.00)	-0.28335	-0.28335	0.00000
		1	0	4S	1(0.00)	-0.45444	-0.45444	0.00000
	PZ	2	1	3P	1(6.00)	-1.83622	-1.83622	0.00000
		3	2	3D	1(0.00)	-0.28975	-0.28975	0.00000
			1	0	4S	1(0.00)	-0.44778	-0.44778
Rb		2	1	4P	1(6.00)	-1.59127	-1.59128	0.00001
	PBE	2	0	5S	1(0.00)	-0.44447	-0.44453	0.00006
		3	2	4D	1(0.00)	-0.27500	-0.27499	0.00001
	PZ	2	1	4P	1(6.00)	-1.60172	-1.60173	0.00001
		2	0	5S	1(0.00)	-0.44245	-0.44255	0.00009
			3	2	4D	1(0.00)	-0.27829	-0.27827
Cs		2	1	5P	1(6.00)	-1.37222	-1.37223	0.00000
	PBE	2	0	6S	1(0.00)	-0.41445	-0.41445	0.00000
		3	2	5D	1(0.00)	-0.32319	-0.32319	0.00000
	PZ	2	1	5P	1(6.00)	-1.38411	-1.38412	0.00000
		2	0	6S	1(0.00)	-0.41523	-0.41523	0.00000
			3	2	5D	1(0.00)	-0.32893	-0.32893

TABLE III. Phonon frequencies (cm^{-1}) of H_g modes at the Γ point calculated by density functional perturbation theory (DFPT) with LDA and PBE exchange-correlation functionals (denoted by superscripts L and P in the first column, respectively) compared with the results of calculations by Nomura and Arita⁴ and experimental frequencies.

Mode	DFT									exp.			
	present						Nomura et al						
	K ₃ C ₆₀		Rb ₃ C ₆₀		Cs ₃ C ₆₀		K ₃ C ₆₀		Rb ₃ C ₆₀		Cs ₃ C ₆₀		
E _g	T _g	E _g	T _g	E _g	T _g	E _g	T _g	E _g	T _g	E _g	T _g	E _g	T _g
$H_g^L(1)$	257	269	256	266	254	265	257, 268	255, 267	256,277				
$H_g^P(1)$	257	274	256	271	252	267	–	–	–	268 ^a	263 ^b , 265 ^c	–	
$H_g^L(2)$	407	403	404	403	394	397	423, 425	422, 423	422, 425				
$H_g^P(2)$	406	401	399	402	391	391	–	–	–	416 ^a	415 ^b , 395 ^c	418 ^b	
$H_g^L(3)$	653	657	660	658	649	650	683, 686	683, 686	686, 688				
$H_g^P(3)$	637	642	636	641	629	632	–	–	–	712 ^a	713 ^c	–	
$H_g^L(4)$	777	778	771	769	772	768	777, 778	777, 778	780, 788				
$H_g^P(4)$	770	768	762	758	761	755	–	–	–	752 ^a	749 ^b , 743 ^c	–	
$H_g^L(5)$	1107	1103	1096	1090	1093	1085	1110,1114	1110,1114	1116,1125				
$H_g^P(5)$	1094	1087	1071	1081	1076	1065	–	–	–	–	–	–	
$H_g^L(6)$	1270	1263	1246	1240	1241	1237	1267,1273	1267,1272	1277,1283				
$H_g^P(6)$	1251	1240	1224	1216	1217	1211	–	–	–	–	–	–	
$H_g^L(7)$	1382	1380	1361	1363	1357	1354	1402,1407	1403,1405	1415,1415				
$H_g^P(7)$	1357	1353	1333	1334	1327	1323	–	–	–	1409 ^a	–	–	
$H_g^L(8)$	1521	1518	1512	1515	1512	1515	1531,1536	1531,1535	1541,1544				
$H_g^P(8)$	1499	1497	1486	1491	1484	1488	–	–	–	1550 ^a	–	–	

^a Ref.⁶

^b Ref.^{7,8}

^c Ref.⁹

TABLE X. Effective frequencies extracted from corresponding elastic response parameters ζ , compared with the frequencies of isolated C_{60} (in cm^{-1}). Calculations are done with LDA and PBE (in the parentheses) functionals.

		K_3C_{60}	Rb_3C_{60}	Cs_3C_{60}	Cs_3C_{60} (A15)	Isolated C_{60}
IntraC60	$A_g(1)$	497(488)	492(490)	491(488)	496(489)	496
	$A_g(2)$	1468(1427)	1448(1440)	1446(1438)	1472(1444)	1470
	$H_g(1)$	256(254)	255(255)	253(251)	254(252)	273
	$H_g(2)$	403(402)	402(399)	394(390)	398(393)	437
	$H_g(3)$	653(641)	656(639)	649(630)	656(636)	710
	$H_g(4)$	765(748)	755(748)	749(740)	755(742)	774
	$H_g(5)$	1104(1078)	1093(1078)	1088(1071)	1092(1076)	1099
	$H_g(6)$	1279(1233)	1256(1234)	1254(1229)	1257(1232)	1250
	$H_g(7)$	1335(1285)	1301(1275)	1270(1239)	1289(1253)	1428
	$H_g(8)$	1455(1407)	1427(1399)	1400(1365)	1418(1380)	1575
Akali:cube	A_g	116(97)	83(99)	65(74)	-	-
	E_g	111(96)	78(93)	61(70)	-	-
	$T_{2g}(1)$	104(93)	73(86)	55(63)	-	-
	$T_{2g}(2)$	107(95)	76(88)	58(66)	-	-
Akali:oct	A_g	32(39)	17(58)	11(27)	-	-
	E_g	28(46)	16(49)	11(26)	-	-
	T_{2g}	30(41)	17(54)	12(26)	-	-
Akali:poct	$A_g(1)$	-	-	-	36(37)	-
	$A_g(2)$	-	-	-	40(40)	-
	$E_g(1)$	-	-	-	51(52)	-
	$E_g(2)$	-	-	-	32(32)	-
	$T_{2g}(1)$	-	-	-	48(55)	-
	$T_{2g}(2)$	-	-	-	43(49)	-
	$T_{2g}(3)$	-	-	-	44(51)	-
InerC60:FCC	$A_g(1)$	43(49)	43(53)	39(48)	-	-
	$E_g(1)$	35(35)	32(41)	26(33)	-	-
	$E_g(2)$	35(36)	33(42)	29(35)	-	-
	$T_{2g}(1)$	34(35)	33(41)	28(34)	-	-
	$T_{2g}(2)$	40(43)	39(48)	34(42)	-	-
InerC60:A15	$A_g(1)$	-	-	-	21(24)	-
	$E_g(1)$	-	-	-	21(24)	-
	$T_{2g}(1)$	-	-	-	29(32)	-
	$T_{2g}(2)$	-	-	-	31(34)	-